The Inner Resonance Ring of NGC 3081. II. Star Formation, Bar Strength, Disk Surface Mass Density, and Mass-to-Light Ratio

Gene G. Byrd – University of Alabama

Tarsh Freeman – Bevill State Community College

Ronald J. Buta – University of Alabama

Citation of published version:

Byrd, G., Freeman, T., Buta, R. (2006): The Inner Resonance Ring of NGC 3081. II. Star Formation, Bar Strength, Disk Surface Mass Density, and Mass-to-Light Ratio. *The Astronomical Journal*, 131(3).
DOI: 10.1086/499944

The Astronomical Journal, 131:1377–1393, 2006 March

THE INNER RESONANCE RING OF NGC 3081. II. STAR FORMATION, BAR STRENGTH, DISK SURFACE MASS DENSITY, AND MASS-TO-LIGHT RATIO

Gene G. Byrd,[1] Tarsh Freeman,[2] and Ronald J. Buta[1]
Received 2005 July 19; accepted 2005 November 19

ABSTRACT

We complement our *Hubble Space Telescope* (*HST*) observations of the inner ring of the galaxy NGC 3081 using an analytical approach and *n*-body simulations. We find that a gas cloud inner (r) ring forms under a rotating bar perturbation with very strong azimuthal cloud crowding where the ring crosses the bar major axis. Thus, star formation results near to and "downstream" of the major axis. From the dust distribution and radial velocities, the disk rotates counterclockwise (CCW) on the sky like the bar pattern speed. We explain the observed CCW color asymmetry crossing the major axis as due to the increasing age of stellar associations inside the r ring major axis. These move faster than the pattern speed. The exterior point of the r ring at the bar major axis has an orbital rate equal to the pattern speed. We show how the perturbation strength can be estimated from the ring shapes and relative spacing over the inner through outer ring regions. The bar strength (maximum tangential/radial force) appears to be constant from 6 to 15 kpc. We derive how the perturbation, the fractional long wavelength $m = 2$ intensity, and the rotation curve can be used to calculate the disk surface mass density versus radius. The disk surface density at 7 kpc is 13 $M_{\odot}$ pc^{-2} rising to 19 at 13 kpc. The latter is insufficient by a factor of seven to generate the observed rotation curve, implying halo domination. The surface density may have been reduced at 7 kpc due to inner ring gas cloud scattering. The surface density plus the observed surface brightness gives a disk mass-to-light (M/L) ratio which increases from 7 kpc through 13 kpc, contradicting the usual assumption in bar strength calculations. The simulation ring lifetime of several billion years is consistent with our ~400 Myr *HST* estimates. With a sufficiently high gas cloud surface mass density, our simulations form gas cloud "associations" near the ends of the bar as observed. Too high a density destroys the ring.

Key words: galaxies: individual (NGC 3081) — galaxies: structure

1. INTRODUCTION

Ringed galaxies stand out as some of the most remarkable morphologies among the general disk galaxy population. Rings are in sufficient abundance, and have such distinctive characteristics, that they have been the subject of numerous observational and theoretical investigations (e.g., Buta 1995, 1999, 2002; Patsis et al. 2003; Kormendy & Kennicutt 2004). The results of these studies suggest that observed rings are linked to orbit resonances in the disk plane of a barred galaxy, where gas is accumulated through the action of gravity torques due to the bar (Buta & Combes 1996).

A unified theory of ring formation in terms of orbits was outlined by Regan & Teuben (2004). They argued against the general term "resonance ring," at least for inner and nuclear rings, because in strongly barred galaxies the concept means less, since the epicyclic definition of resonance locations breaks down completely. In particular, the inner Lindblad resonance may not even exist in a strongly barred galaxy, and yet a nuclear ring, often linked to this resonance (e.g., Buta & Crocker 1993), is still observed. Contopoulos (1996) outlines the nonlinear definition of inner Lindblad resonances in galaxies and has argued that even in strong bars, one may speak of "resonance regions." It is in these regions that the orbit families required for ring formation are found, and therefore studying rings in terms of orbits is an approach worth considering.

There is still much that is not known about galactic rings, particularly the mechanism of star formation in such features and how this relates to orbit dynamics. In Paper I (Buta et al. 2004a), we presented an analysis of *Hubble Space Telescope* (*HST*) *UBVI* images of the inner ring of NGC 3081, a classic early-type spiral with one of the most distinctive multiring morphologies among the general galaxy population. NGC 3081 is an especially good candidate for studies of star formation in rings because of several unique features (Buta & Purcell 1998). The galaxy has four well-defined, nested, and virtually closed ring features (Fig. 1), denoted, from smallest to largest, the nuclear ring (nr), the inner ring (r), and the R_1 and R_2 outer rings. Each is defined by active star formation, with little or no star formation being found between the rings.

The rings are in each case intrinsically elongated and show alternating ~0° and 90° major axis alignments with respect to the bar. The rings strongly resemble the periodic orbits that would exist in a weak bar potential near specific orbit resonances, based on both analytic (Contopoulos 1979; Freeman & Byrd 2000) and numerical studies (Schwarz 1981, 1984; Byrd et al. 1994; Rautiainen & Salo 2000; Buta & Combes 1996, 2000; Regan & Teuben 2004). Paper I argued that these characteristics imply that NGC 3081 has been evolving in a relatively undisturbed manner for much of a Hubble time. In the presence of galaxy interactions, it is unlikely that ring material could gather in such an extremely well organized manner (e.g., Schwarz 1981). Thus, the star formation in the rings of NGC 3081 must be largely a problem of internal dynamics.

In Paper I, we focused on star formation in the inner ring because this feature has the highest contrast and most distinctive characteristics of the galaxy's four major rings. In the *HST* images

[1] Department of Physics, and Astronomy Department, University of Alabama, Tuscaloosa, AL 35487.
[2] Bevill State Community College, Jasper, AL.

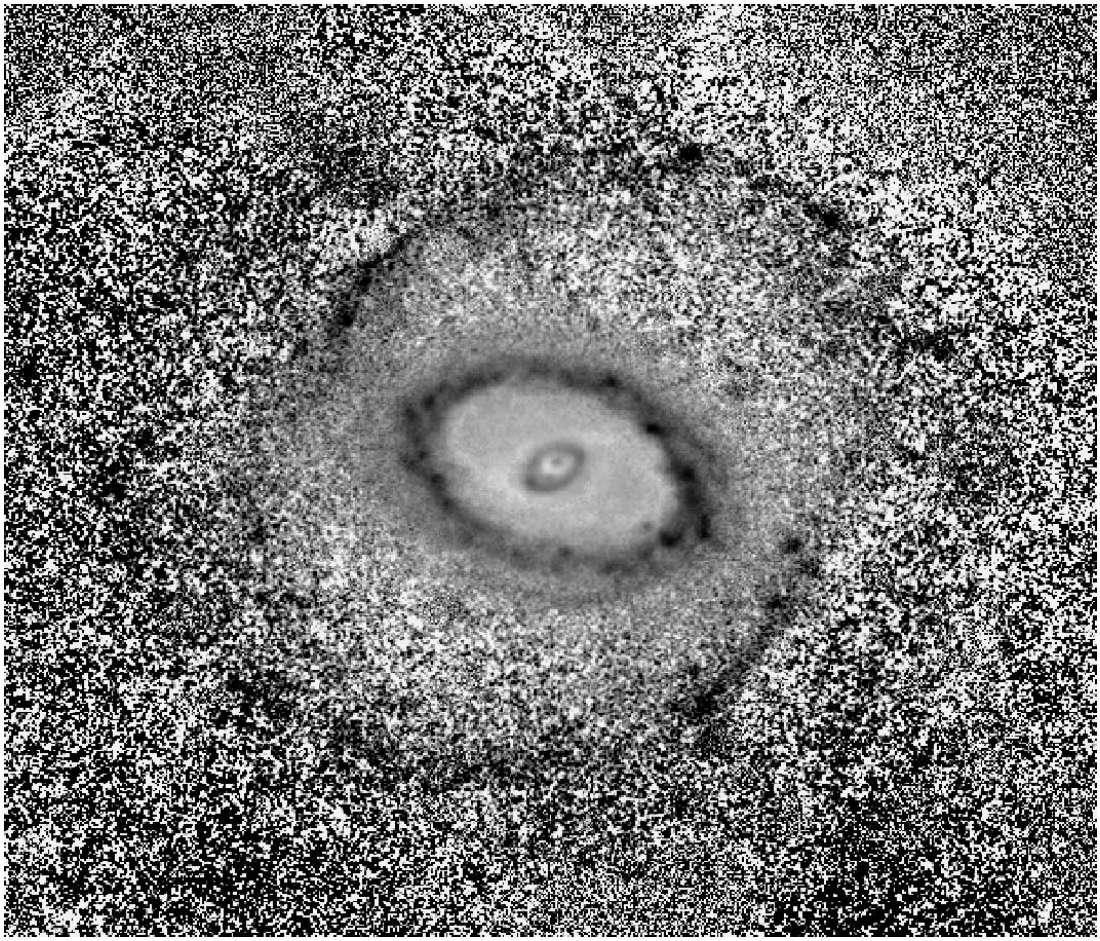

FIG. 1.—$B-I$ color index map of NGC 3081. Blue is represented by dark gray, and red by lighter shades. Note the small nuclear (nr) ring, inner r ring, and large outer R_1, R_2 rings. The disk turns CCW on the sky. The outer long dimension of r ring is about 38″.5 (7 kpc). NGC 3081 is tilted about 34°, with a 97° line of nodes position angle.

(Fig. 2), the ring is well-resolved into young clusters and associations, and fits completely within the Wide Field and Planetary Camera 2 (WFPC2) field of view. Our goal is to try and account for several features of this ring:

1. Its intrinsically elongated shape (axis ratio ≈0.7), alignment parallel to the bar axis, and its major axis location relative to the locations of the minor axis of the outer R_1 ring and the major axis of the R_2 ring on the bar axis (Figs. 1 and 2).
2. The strong concentration of young clusters and the more luminous associations, mainly around the ends of the ring major axis, coinciding with the bar axis. Also, the fact that some possibly very old clusters are found at the ends of the bar (Figs. 3 and 4).
3. The tendency for star formation in the ring to slightly lead the bar (see Figs. 3 and 4).
4. The photometric properties of the near-infrared disk, i.e., the maximum amplitude and phase of the $m = 2$ Fourier component relative to the $m = 0$ component near the inner ring major axis radius, as well as the exponentially declining surface brightness of the disk with radius (Figs. 5 and 6).

Our approach to these questions is largely analytic and in terms of orbits, supplemented by numerical simulations. Analytic modeling can complement numerical simulations, considering the difference between the analytic simplifying assumptions and the simulation limitations, such as particle number and the resulting need for force law softening (see, e.g., Byrd 1995, and references therein). The analytic discussion is for an infinite particle number; the analytic approach assumes small perturbations, while the simulations do not.

2. NOTATION

We use notation similar to that in Binney & Tremaine (1987, hereafter BT), in particular the derivation of their equations (3-107) and (3-118). The parameter Ω_0 is the undisturbed circular angular velocity, which can vary with radius, and Ω_p is the pattern speed or angular rate at which the perturbing potential turns (constant with radius). Angular velocities are positive in the counterclockwise (CCW) sense, and the major axis of the bar perturbation is along the x-axis in a standard Cartesian coordinate system with $+x$ to the right, $+y$ upward, and $+z$ out toward the reader. Disk objects in undisturbed circular motion have an angular velocity relative to the bar of

$$\frac{d\phi}{dt} = (\Omega_0 - \Omega_p). \tag{1}$$

The bar perturbs disk objects from a circular orbit radius, r_0, by

$$r_1 = r - r_0, \tag{2a}$$

$$\phi_1 = \phi - \phi_0, \tag{2b}$$

where ϕ_0 is a reference angle for undisturbed motion and ϕ is the angle from the bar. Kalnajs (1991) qualitatively discussed how

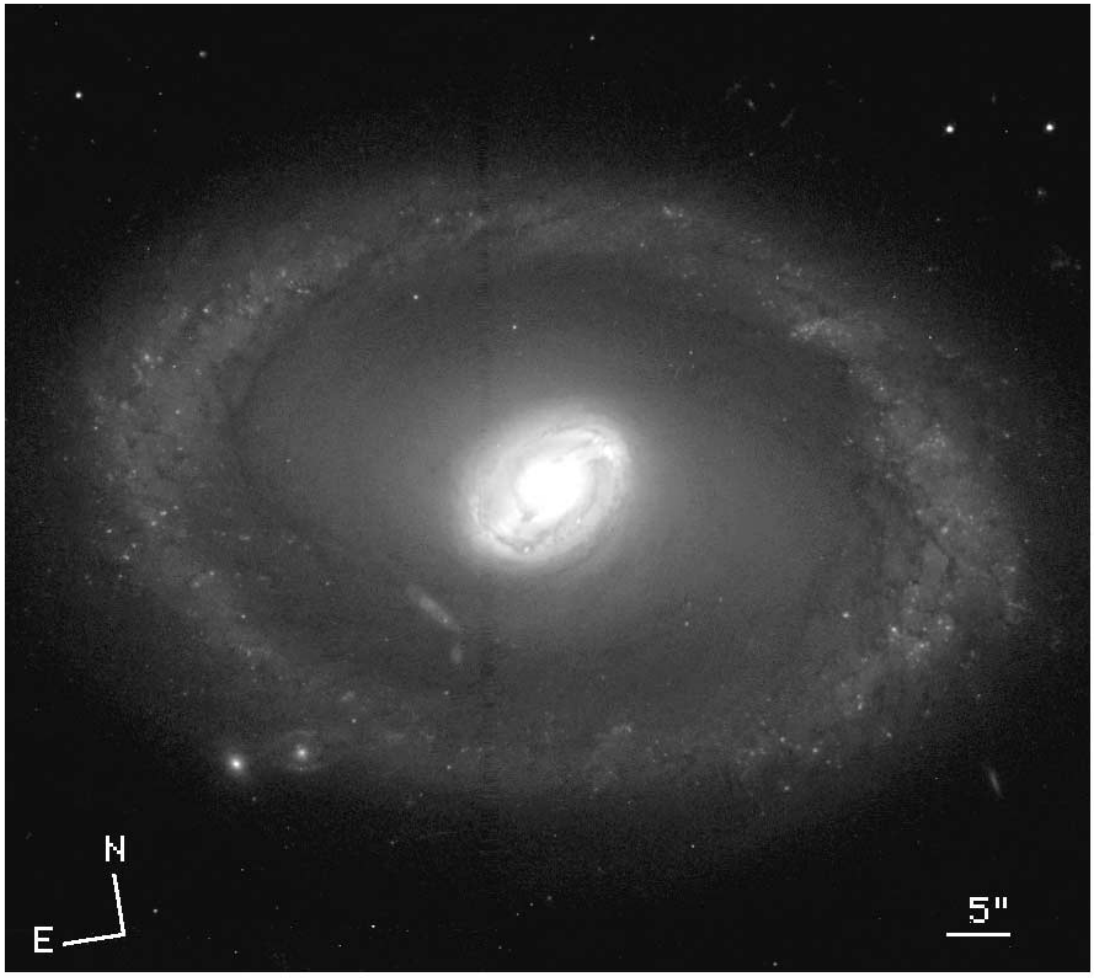

FIG. 2.—*HST* image of NGC 3081, showing central region of Fig. 1. Note the small nuclear (nr) ring, larger inner (r) ring, and the individual associations in the inner ring.

perturbations should send disk gas clouds into noncircular orbits, which will be damped by collisions with adjoining clouds or a diffuse medium. Mass recycling from stars, etc., should replenish the diffuse medium to provide a small amount of long-term drag on the gas clouds, and contribute to the formation of new clouds. Here we extend Kalnajs's discussion by focusing on the inner ring of NGC 3081 and analytically including the dynamical effects of

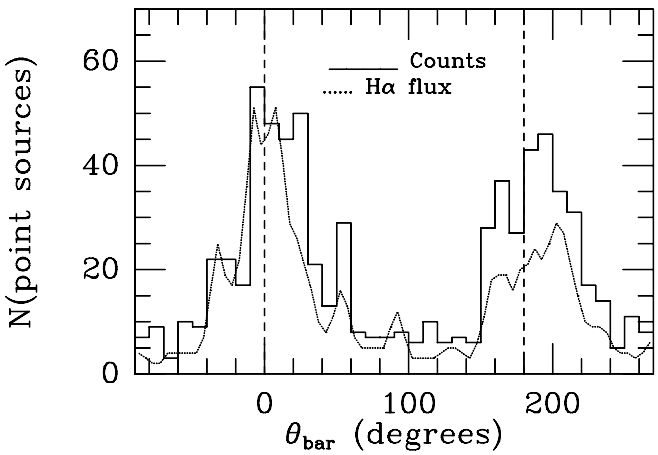

FIG. 3.—*HST* association number histogram vs. angle around the ring in the galaxy plane (Buta et al. 2004a). Note CCW asymmetry of the peaks in number and Hα young association emission (*dotted line*) at the bar ends (*dashed line*).

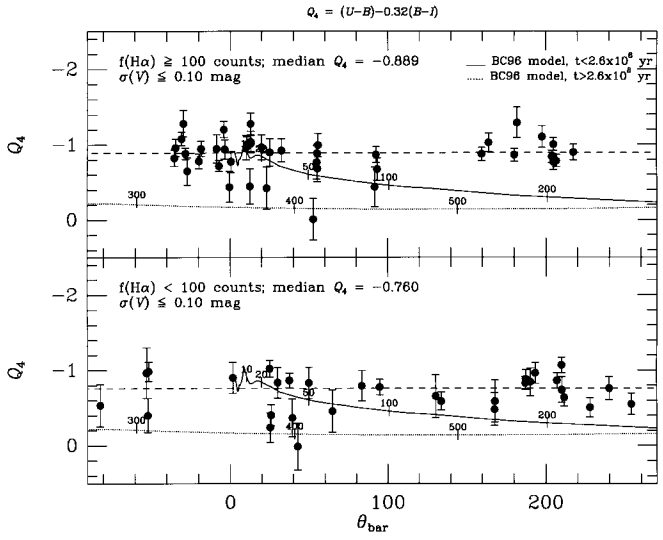

FIG. 4.—Reddening-free age index $Q_4 = (U - B) - 0.32(B - I)$ vs. angle around the ring in the galaxy plane (Buta et al. 2004a). The sloping solid line indicates the Q_4 age, with 1° on the horizontal axis equal to 10^6 yr, starting with 0 at 0°. Tick marks on the solid line show Q_4 age values in Myr, calculated from Bruzual & Charlot (1996). Top graph shows younger (more negative Q_4 and higher Hα emission) associations, and the bottom graph shows older (less negative Q_4 lower Hα emission) associations. Note the larger phase shift in the CCW sense from bar ends at 0° and 180° for older associations, and the smaller shift for younger associations. Also note that some associations could be 400 Myr old.

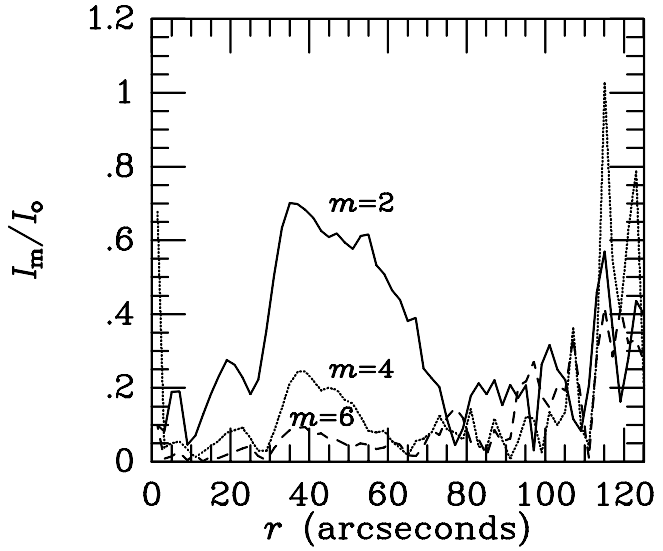

FIG. 5.—*H*-band I_m/I_0 component ratio for the NGC 3081 disk. Note that the maximum of I_2/I_0 vs. radius occurs near the inner ring radius, with a decline to small values at larger radii. Note how smooth and well-defined this curve is over the 35″ –80″ range of the inner, r, and outer, R_1, rings. Also note the dominance of the twofold over other components.

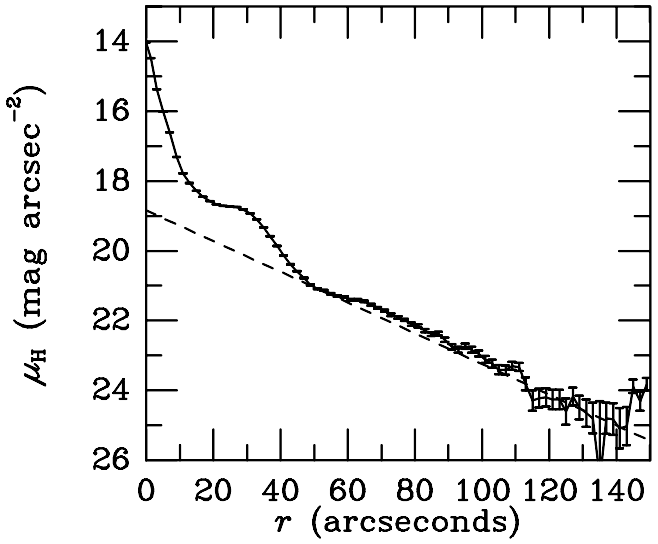

FIG. 6.—*H*-band I_0 vs. radius for the NGC 3081 disk. Note the "shoulder" or "lens" in the neighborhood of the inner ring and corotation with a simple exponential decline beyond that.

this damping in the equations of motion. We adopt a procedure similar to that used by Goldreich & Tremaine (1981, § IIIb) for the rings of Uranus. The change due to damping in the peculiar velocity vector, $\boldsymbol{v}_1$, per unit time is a positive constant, c, times the negative of the peculiar velocity vector whose components are

$$-c\frac{dr_1}{dt} \text{ and } -cr_0\frac{d\phi_1}{dt}. \tag{3}$$

Both of these terms are added to the right-hand side of the equations of motion, like equations (3-107a,b) in BT.

We denote Φ as the net original plus perturbation potential and Φ_0 as the circularly symmetric, unperturbed potential evaluated at r_0; $\Phi^A_{p,m}$ is then the amplitude of the azimuthal component of the disturbing potential of multiplicity m. We consider a bar here to be mainly a twofold ($m = 2$) perturbation, which should be adequate for NGC 3081, because its primary bar is relatively weak (see, e.g., Buta & Block 2001). The pattern rate is presumed to be the same for all Fourier components. Consider the effect of each m-fold Fourier component of the perturbing potential, $\Phi_{p,m}$, separately, such that

$$\Phi = \Phi_0 + \Phi_{p,m} = \Phi_0 + \Phi^A_{p,m}\cos(m\phi). \tag{4}$$

3. DAMPED, FORCED MOTION

We use Binney & Tremaine's (1987) oscillator equations (3-116a) and (3-116b) for forced, undamped radial and azimuthal motions of an orbiting particle in the disk of a galaxy. However, we modify the equations by adding dissipation terms,

$$\frac{d^2r_1}{dt^2} + \left(\frac{d^2\Phi_0}{dr^2} - \Omega^2\right)_0 r_1 - 2r_0\Omega_0\frac{d\phi_1}{dt} + c\frac{dr_1}{dt} = -\left(\frac{\partial\Phi_{p,m}}{\partial r}\right)_{r_0}\cos(m\phi), \tag{5a}$$

$$\frac{d^2\phi_1}{dt^2} + 2\frac{\Omega_0}{r_0}\frac{dr_1}{dt} + c\frac{d\phi_1}{dt} = \left(\frac{m\Phi^A_{p,m}}{r_0^2}\right)\sin(m\phi). \tag{5b}$$

A particle with no velocity perturbations located slightly ahead of the bar should be decelerated by the bar. Since acceleration is the negative gradient of the potential, we thus must have

$$\Phi^A_{p,m} < 0. \tag{6}$$

Corotation (CR) is where $\Omega_0 = \Omega_p$. The inner ring is thought to occur inside CR, where $(\Omega_0 - \Omega_p) > 0$ for a typical constant circular velocity rotation curve (e.g., Buta & Purcell 1998). The epicyclic frequency κ is defined as usual (e.g., BT eq. [3-118b]).

4. SOLUTIONS NEAR LINDBLAD RESONANCES (NEAR-LR)

4.1. *The Near-LR Solutions*

This derivation will follow that of BT's equations (3-107) and (3-119), but with damping. Here we assume $(\Omega_0 - \Omega_p)t = \phi_0 = \phi$ in the sine and cosine terms. This assumption is appropriate for regions where the angular perturbations are not large near to but not at Lindblad resonances (near-LR). We define the LR below. This assumption is *not* appropriate for points near or at corotation (CR), where the unperturbed orbital speed is equal to the perturbation pattern speed. Since we are well away from CR, we can take $cd\phi_1/dt$ to be small in equation (5b), solve for $d^2\,\phi_1/dt^2$, and integrate; then we obtain BT equation (3-117),

$$\left(\frac{d\phi_1}{dt}\right)_{\rm LR} = -2\frac{\Omega_0}{r_0}r_1 - \left[\frac{\Phi^A_{p,m}}{r_0^2(\Omega_0 - \Omega_p)}\right]_0\cos[m(\Omega_0 - \Omega_p)t]. \tag{7}$$

Substituting in equation (5a) and for the epicyclic frequency, we obtain BT equation (3-118a), but with damping,

$$\frac{d^2r_1}{dt^2} + c\frac{dr_1}{dt} + \kappa^2 r_1 = -\left[2\Omega_0\frac{\Phi^A_{p,m}}{r_0(\Omega_0 - \Omega_p)} + \frac{\partial\Phi_{p,m}}{\partial r}\right]_0\cos[m(\Omega_0 - \Omega_p)t]. \tag{8}$$

We follow standard procedure to obtain a solution (e.g., Arfken 1985, p. 712). For the solution, we obtain BTs equation (3-119), but with damping added:

$$r_{1,\mathrm{LR}} = -\left[\frac{\partial \Phi_{p,m}}{\partial r} + 2\Omega_0 \frac{\Phi^A_{p,m}}{r_0(\Omega_0 - \Omega_p)}\right]_0 \frac{\cos\left[m(\Omega_0 - \Omega_p)t - \eta\right]}{\sqrt{\Delta^2 + m^2(\Omega_0 - \Omega_p)^2 c^2}}, \tag{9}$$

where

$$\Delta = \left|\kappa^2 - m^2(\Omega_0 - \Omega_p)^2\right|. \tag{10}$$

Assuming $(\Omega_0 - \Omega_p)t = \phi_0$, the phase angle in equation (9) is given by

$$\tan\eta = \frac{m(\Omega_0 - \Omega_p)c}{\kappa^2 - m^2(\Omega_0 - \Omega_p)^2}. \tag{11}$$

4.2. *Near-LR Angle Perturbation and Orbit Shapes*

Assuming $(\Omega_0 - \Omega_p)t = \phi$, we get a solution for ϕ_1 by integrating the $d\phi_1/dt$ (eq. [7]). First, we must integrate equation (9). Simplifying the integral of r_1, substituting it, and integrating the other term in the $d\phi_1/dt$ equation, we get

$$\phi_{1,\mathrm{LR}} = \frac{2\Omega_0}{r_0}\left[\frac{\partial \Phi_{p,m}}{\partial r} + 2\Omega_0 \frac{\Phi^A_{p,m}}{r_0(\Omega_0 - \Omega_p)}\right]_0 \times \frac{1}{m(\Omega_0 - \Omega_p)} \frac{\sin\left[m(\Omega_0 - \Omega_p)t - \eta\right]}{\sqrt{\Delta^2 + m^2(\Omega_0 - \Omega_p)^2 c^2}} + \frac{\Phi_{p,m}}{r_0^2} \frac{\sin\left[m(\Omega_0 - \Omega_p)t\right]}{m(\Omega_0 - \Omega_p)^2}. \tag{12}$$

We assume that the perturbation potential amplitude of NGC 3081 is nearly constant with radius from the inner through the outer rings, so the partial derivative of the amplitude with radius is zero. The shapes (smaller/larger radii) of the inner compared to the two outer rings of NGC 3081 support this assumption. Assuming $(\Omega_0 - \Omega_p)t = \phi_0$, we see that with small damping, equation (11) gives $\tan\eta \approx 0$. The radial perturbation given by equation (10) for small damping has an amplitude $C_{r,m}$. Since $\Phi^A_{p,m} < 0$ and $(\Omega_0 - \Omega_p) > 0$ inside CR, $C_{r,m} > 0$, so that the periodic orbits are elongated with $r_1 > 0$ along the bar. For small perturbations, $m = 2$ orbits will be elongated, with a semimajor axis of $r_0 + C_{r,2}$ and a semiminor axis of $r_0 - C_{r,2}$. Outside CR, the orbits are elongated 90° to the bar.

4.3. *Lindblad Resonances*

Let r_{CR} be the corotation radius. At higher order resonances than CR, $\Delta^2 = 0$ corresponds to the BT equation (3-122). The Lindblad resonances (LRs) occur where $\Delta = 0$ for $m = 2$. Inside CR, this corresponds to the inner Lindblad resonance (ILR), while outside CR it corresponds to the outer Lindblad resonance (OLR). Near the Lindblad resonances, the square root in the r_1 and ϕ_1 equations above becomes very small, and r_1 or ϕ_1 can become large. For $m = 2$, the smaller radius, r_0, where this can occur is the ILR. Based on previous studies, we may deduce that the nuclear ring of NGC 3081 is likely to lie within $\Delta = 0$ with $m = 2$, defined as the ILR, while the inner ring lies between CR and ILR. Taking a flat rotation curve and CR to be 51″.5 for NGC 3081 and the above definitions, the ILR is at 15″, and the OLR would be at 87″.9.

We assume for the inner ring that damping is small, as seen by the alignment of the inner ring along the bar. This is not the case for the nuclear ring, whose intrinsic major axis is oriented 71° to the bar axis (Buta & Purcell 1998). Within the context of our analytic model, this implies that the nuclear ring has a lot of damping. In contrast, the inner ring and the two outer R rings of NGC 3081, when deprojected (see Fig. 11 and Table 5 of Buta & Purcell 1998), show approximately parallel and perpendicular alignments with respect to the bar, which indicates no damping in the analytic models.

5. SOLUTION NEAR TO COROTATION (NEAR-CR)

5.1. *Near-CR Pendulum Behavior and Variables*

In the above solutions, we assumed that the angular rate of the particles is not greatly changed. However, this may not be the case, particularly near CR. Here we examine this region, in which the inner (r) ring and outer R_1 ring of NGC 3081 are located. As BT show (their eqs. [3-127]–[3-129]), the r_1 amplitude remains finite even at CR, since the motion at this point is the well-known pendulum oscillator equation (BT eq. [3-127b]), not the oscillator equation. They show that very near CR, the particles oscillate about points 90° to the bar in banana-shaped loops.

For particles closer in to the center than CR and also farther out beyond CR, the motion is again like a pendulum around these points, but corresponding to behavior above a critical energy. We go beyond BT and derive the circulating path about the disk center corresponding to the inner and outer rings.

Because the motion is referenced to the 90° angle and is a pendulum oscillation, we denote it with a subscript "pen" and different angular variables,

$$\phi = \phi_0 + \phi_{1,\mathrm{pen}} = \pi/2 + \phi_{1,\mathrm{pen}}. \tag{13a}$$

Note that this is different from equation (2b) in the earlier LR section. For the pendulum case, the reference radial distance will be r_0, and

$$r = r_0 + r_{1,\mathrm{pen}}. \tag{13b}$$

5.2. *Near-CR Solution for Perturbed Motion*

In equation (5a), we drop as small terms $d^2 r_{1,\mathrm{pen}}/dt^2$, $c dr_1/dt$, and the partial derivative term. We also include κ in the equation and solve for the time derivative of the perturbation angle,

$$\left(\frac{d\phi_1}{dt}\right)_{\mathrm{pen}} = \left(\kappa^2 - 4\Omega^2\right)_0 \frac{r_{1,\mathrm{pen}}}{2r_0\Omega_0}. \tag{14}$$

A general expression for the radial velocity perturbation can be obtained that does not assume $(\Omega_0 - \Omega_p)t = \phi$. We obtain this by dropping the first and third left-hand terms in equation (5b) and solving for the radial velocity perturbation,

$$\left(\frac{dr_1}{dt}\right)_{\mathrm{pen}} = \frac{1}{2\Omega_0}\left(\frac{m\Phi^A_{p,m}}{r_0}\right)_0 \sin(m\phi). \tag{15}$$

Taking the derivative of equation (14) and substituting equation (15), we set $\psi = 2\phi_{1,\mathrm{pen}}$ and

$$p^2 = \left|\frac{4}{r_0^2}\Phi^A_{p,m}\right|_0 \left(\frac{4\Omega_0^2 - \kappa^2}{\kappa^2}\right)_0. \tag{16}$$

We obtain the pendulum oscillator equation of motion,

$$\frac{d^2\psi}{dt^2} = -p^2 \sin\psi. \tag{17}$$

The integral of motion is

$$E_{\rm pen} = \frac{1}{2}\left(\frac{d\psi}{dt}\right)_0^2 - p^2\cos\psi. \tag{18}$$

Particles in the inner ring circulate instead of oscillating, so we must have $E_{\rm pen} > p^2$. Examining the value of the integral equation for $\cos\psi = 0$ and also where p^2 approaches zero, we obtain

$$E_{\rm pen} = \tfrac{1}{2}\left[2(\Omega_0 - \Omega_p)\right]^2 = 2(\Omega_0 - \Omega_p)^2. \tag{19}$$

We require for the inner ring particles, which circulate around relative to the bar,

$$2(\Omega_0 - \Omega_p)^2 > \frac{4}{r_0^2}|\Phi^A_{p,m}|_0\left(\frac{4\Omega^2 - \kappa^2}{\kappa^2}\right)_0. \tag{20}$$

We use equations (16), (17), (18), (19), and (20) to obtain $\frac{1}{2}(d\psi/dt)^2 = 2(d\phi_{1,\rm pen}/dt)^2$. We get the equation for the angular velocity perturbation,

$$\left(\frac{d\phi_1}{dt}\right)_{\rm pen} = \pm\sqrt{(\Omega_0 - \Omega_p)^2 + \frac{2}{r_0^2}|\Phi_{p,m}|_0\left(\frac{4\Omega^2 - \kappa^2}{\kappa^2}\right)_0\cos 2\phi_{1,\rm pen}}, \tag{21a}$$

where the upper plus sign corresponds to points inside CR for the inner ring and the lower negative sign is for points outside CR for the outer R_1 ring. Note that if the perturbation were made to equal zero,

$$\left(\frac{d\phi_1}{dt}\right)_{\rm pen} = \begin{cases} \left(\Omega_0 - \Omega_p\right)_r > 0 & \text{inside CR,} \\ \left(\Omega_0 - \Omega_p\right)_R < 0 & \text{outside CR.} \end{cases}$$

We substitute equation (21a) into the $d\phi_{1,\rm CR}/dt$ equation (14) and solve for

$$r_{1,\rm pen} = -\frac{2r_0\Omega_0 d\phi_{1,0}/dt}{(4\Omega^2 - \kappa^2)_0} = \pm\left(\frac{2r\Omega}{4\Omega^2 - \kappa^2}\right)_0 \times\sqrt{(\Omega_0 - \Omega_p)^2 + \left(\frac{2}{r^2}|\Phi^A_{p,m}|\frac{4\Omega^2 - \kappa^2}{\kappa^2}\right)_0\cos 2\phi_{1,\rm pen}}, \tag{21b}$$

where the plus sign corresponds to points outside CR, and the minus to points inside CR. The above equation is like BT's equation (3-129), except we are considering a particle circulating (not oscillating) relative to the bar. Here note that if the perturbation approaches zero or if r_0 is well inside CR, we have a constant minus or plus r_1, and the motion is circular. The radial distance from the center is $r = r_0 + r_{1,\rm pen}$ from equation (13b) for the pendulum oscillator case. Inside CR, the smallest $r_1 = 0$ and the largest $r = r_0$ along the bar at $\phi_{1,\rm pen} = \pm\pi/2$. The largest r_1 and the smallest r is at $\phi_{1,\rm pen} = 0$ along the minor axis of the bar. The orbits inside CR are thus elongated along the bar inside and near to CR. We shall see that the major-axis ends of the ring are pointed, and there is transverse crowding at the major axis corresponding to observations. The reverse elongation is true for points outside CR, with the short dimension along the bar.

We can use our results to plot the periodic orbits of the inner (r) ring and the outer (R_1) ring. Below, we just give the r versions of the equations, unless stated otherwise. We can specify r_0, $r_{\rm CR}$, Ω_0, and $\Phi_{p,m}$, and obtain $d\phi_1/dt$ along with r_1. We can then via a simple numerical procedure obtain the time interval between close neighboring ϕ_0 values. We obtain r_1 by equation (21b) and then $d\phi_1/dt$ by equation (14). The corresponding angular interval for a given time change is

$$\Delta\phi = \Delta t\left(\frac{d\phi_1}{dt}\right). \tag{22}$$

6. EXAMPLE POTENTIAL

For examples of these orbits, we use an axisymmetric potential similar to one used in Binney & Tremaine (1987, eq. [3-77]), which matches the observed flat rotation curve of NGC 3081 (Buta & Purcell 1998),

$$\Phi_0 = \frac{1}{2}V_0^2\ln\left(R_c^2 + r_0^2\right), \tag{23}$$

where the core radius, R_c, is a constant defining the central regions of the galaxy. Equating centrifugal acceleration to

$$\frac{\partial\Phi_0}{\partial r_0} = \frac{r_0 V_0^2}{R_c^2 + r_0^2} \tag{24}$$

gives the rotation curve, V, and the circular angular rate,

$$\Omega_0 = \frac{V}{r_0} = \frac{V_0}{\sqrt{R_c^2 + r_0^2}} \rightarrow \frac{V_0}{r_0} \text{ for } r_0 \gg R_c. \tag{25}$$

This potential also produces a constant rotation speed with radius, $V = V_0$, out in the disk as seen in many galaxies. The flat rotation curve for NGC 3081 gives $V_0 = 221$ km s^{-1} (Buta & Purcell 1998). The circular orbital speed is constant so that the BT equation (3-118b) definition of the epicyclic frequency becomes,

$$\kappa^2 = 2(V_0/r_0)^2. \tag{26}$$

We introduce the amplitude of perturbation potential component m in equation (4) by using a parameter Q that is unity for an axisymmetric potential. For points at radius r along the positive x-axis,

$$\Phi_0 + \Phi^A_{p,m} = \tfrac{1}{2}V_0^2\ln\left(R_c^2 + r^2/Q^2\right). \tag{27}$$

Increasing Q by a small positive quantity q_m gives

$$\Phi^A_{p,m} \approx \frac{\partial\Phi_0}{\partial Q}dQ \approx -V_0^2\frac{r^2 q_m}{R_c^2 + r^2} = -V_0^2 q_m, \tag{28}$$

where the right-hand side is valid well outside the nucleus where $r \gg R_c$. The potential perturbation, $\Phi^A_{p,m}$, is less than zero along

the bar, as we previously deduced. For the region well outside the nucleus,

$$\frac{\partial \Phi_{p,m}}{\partial r} = 0. \tag{29}$$

7. EXAMPLE POTENTIAL OUTER AND INNER RINGS

7.1. *Near-OLR Plot of Rings for Example Potential*

The observed properties of the rings can be used to deduce the perturbing potential by plotting the formulae we have obtained for the example potential using a set of parameters to fit NGC 3081. We will do examples for the flat rotation curve of NGC 3081, $V_0 = 221$ km s^{-1}, and a scale of 100″, equal to about 18 kpc (Buta & Purcell 1998). We take CR to be located at 52.″25, so that the pattern speed is $\Omega_p = 221/52.25 = 4.23$ km s^{-1} arcsec^{-1}.

We first compare a plot of the near-LR equations to the observed rings in NGC 3081. Figure 7 plots $r = r_0 + r_{1,\mathrm{LR}}$ from equations (10) and (14) for small perturbations of the example potential. Here the perturbation $q = 0.035$, with 95% in $m = 2$, $q_2 = 0.033$ and 5% in $m = 4$, $q_4 = 0.002$. This "near-LR" formulation results in an elongated shape for the inner ring within ±40″, which has blunt ends on the major axis. If the perturbation is not small, the major axis ends are even more blunt, and the minor axis points become indented in a peanut shape. Plotting the points at equal times results in a transverse spreading of the points at the major axis and crowding at the minor axis. There appears to be a greater observed concentration of young stellar associations in the ring at the major axis ends, *not* on the minor axis.

As we have discussed earlier, the observed NGC 3081 inner ring, although elongated along the bar, has more pointed ends at the major axis and no dimpling at the minor axis. There is also a greater observed concentration of young stellar associations in the ring at the major axis ends. We thus must use the more accurate "near-CR" formulation for the inner ring and also for the interior edge of the R_1 ring. We will do this in the following sections.

Now, in contrast to the poor LR fit of the properties of the inner ring, we see that the plots in Figure 7 for the exterior edge of the R_1 ring and the interior edge of the R_2 ring (which bracket the OLR) are in excellent agreement with the deprojected version of Figure 1. For the outer part of the ring system to almost 100″ or 18 kpc, $q_2 = 0.033$ and the example potential appears to be a good description. We cannot be sure of the rotation curve near the ILR, but the interior edge of the inner ring and the exterior edge of the nuclear ring appear to match well those in NGC 3081.

7.2. *Near-CR Velocity Perturbations*

Here we obtain general solutions for the perturbations *without* assuming that the transverse angle perturbations are small. We must do this for radii near CR, i.e., in the region of the inner ring and also on the interior edge of the R_1 ring. We make deductions about the velocity perturbations at points around the ring using the observed ring shape, elongated along the bar and compressed at 90° to the bar.

Substituting for the example potential, the equation (14) expression for the tangential angular velocity perturbation becomes

$$\left(\frac{d\phi_1}{dt}\right)_{\mathrm{pen}} = -\frac{\Omega_0 r_{1,\mathrm{pen}}}{r_0} = -\frac{r_{1,\mathrm{pen}}}{r_0^2} V_0. \tag{30}$$

The transverse velocity is equation (30) times r_0. Inside CR, the transverse velocity amplitude increases outward. We see that in general, the tangential velocity perturbation of the normal CCW circular velocity, $(\Omega_0 - \Omega_p)r_0$, is at its largest magnitude clockwise relative to the bar at $\phi = 0°$ and 180°. The tangential velocity perturbation's largest magnitude counterclockwise is at $\phi = 90°$ and 270°. At angles in between these, $\phi = 45°$, 135°, 225°, and 315°, the transverse velocity perturbation is zero.

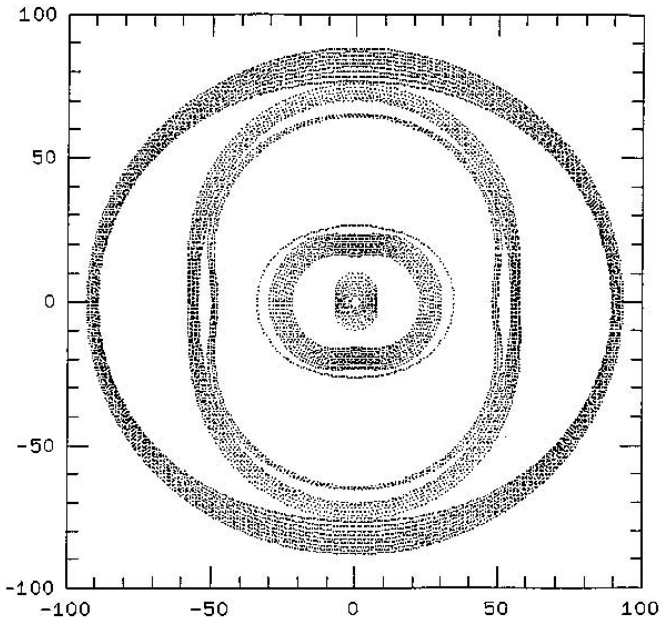

FIG. 7.—Analytic model of NGC 3081 inner and outer rings with LR equations. Perturbation $q_2 = 0.033$, with a small 5% $q_4 = 0.002$ contribution. Note the poor fit for inner ring, but the good fit for the outer edge of the R_1 and inner edge of R_2 outer rings. Compare to Figs. 1 and 2, as seen on the sky and the deprojected Fig. 11 in Buta & Purcell (1998).

Similar to the method of obtaining equation (30), a general expression for the radial velocity perturbation can be obtained that does not assume $(\Omega_0 - \Omega_p)t = \phi$. Equation (15) becomes

$$(dr_1/dt)_{\mathrm{pen}} = -(m/2) q_m V_0 \sin(m\phi). \tag{31}$$

Note that the equation (31) radial velocity perturbation amplitude is approximately constant with radius for the example potential. We see that in general, the radial velocity perturbation has its largest magnitude outward at $\phi = 135°$ and 315°. The radial velocity perturbation's largest magnitude inward is at $\phi = 45°$ and 325°. At angles in between these, $\phi = 0°$, 90°, 180°, and 270°, the radial velocity perturbation is zero.

The small 34° inclination of NGC 3081 results in uncertainties in the exact position angle of NGC 3081's line of nodes (~97°). It is thus difficult to compare theoretical deviations from circularity of ring velocities to observations for this model or others (e.g., Purcell & Buta 1996). On the other hand, the inclination makes comparison of ring shape and location to models easier.

7.3. *Near-CR Radius and Angle Perturbations*

We can define the exterior edge of the inner ring as the largest radius where the clouds circulate around relative to the bar. Closer to r_{CR} than this, the clouds no longer circulate in the ring. Similarly, we define the interior edge of the outer R_1 ring as the smallest radius where the clouds circulate around relative to the bar. Closer to r_{CR} than this, the clouds no longer circulate in the ring.

In equation (16) for the pendulum energy, for the example potential, we can write

$$p^2 = \left(\frac{4}{r_0^2} q_m V_0^2 \frac{2\Omega_0^2}{2\Omega_0^2}\right)_0 = 4 q_m \Omega_0^2. \tag{32}$$

Substituting into equation (21a),

$$\frac{d\phi_{1,\mathrm{pen}}}{dt} = \pm\sqrt{(\Omega_0-\Omega_p)^2+2q_m\Omega_0^2\cos 2\phi_{1,\mathrm{pen}}}$$
$$= \pm\frac{V_0}{r_0}\sqrt{\left(\frac{r_{\mathrm{CR}}-r_0}{r_{\mathrm{CR}}}\right)^2+2q_m\cos 2\phi_{1,\mathrm{pen}}}, \quad (33)$$

where the plus sign corresponds to inside CR and the minus to outside CR for the example potential substituted in equation (21a).

For the example potential, equation (21b) becomes

$$r_{1,\mathrm{pen}} = \pm r_0\sqrt{\left(\frac{r_{\mathrm{CR}}-r_0}{r_{\mathrm{CR}}}\right)^2+2q_m\cos 2\phi_1}$$
$$= \pm r_0\sqrt{2q_m+2q_m\cos 2\phi_1}, \quad (34)$$

where the upper positive sign is for points outside CR and the lower negative sign for points inside CR.

Inside CR for the edge of the inner ring, r_0 is the ring semimajor axis. At the edge of the ring toward CR on the major axis of the ring, the two terms in the square root are of opposite signs and equal magnitudes, so that we have the example potential inner ring solution of equation (34). A similar equation, but with the numerator quantities reversed, results for the outer ring,

$$q_m = [(r_{\mathrm{CR}}-r_0)/(r_{\mathrm{CR}})]^2/2 = [(r_0-r_{\mathrm{CR}})/(r_{\mathrm{CR}})]^2/2. \quad (35)$$

8. NEAR-CR PERTURBATION, RING SHAPES, AND SIZES

The observed properties of the inner ring can be used to deduce the perturbing potential. Recall that for the flat rotation curve for NGC 3081, $V_0 = 221$ km s^{-1}. On the sky 100″ is about 18 kpc (Buta & Purcell 1998). The long and short dimensions of the rings with formulae obtained earlier give the perturbation. Here it is important to note that we need the exterior dimensions of the inner ring. For NGC 3081, the long exterior dimension is 38.″5. For the outer R_1 ring, the short dimension is 64″ and the long 85.″3 (Buta & Purcell 1998, Table 3, footnotes *b* and *d*; see also Fig. 9 of Paper I). From equation (35) and setting $m = 2$, the semimajor axis of the inner ring is

$$38.''5 = r_{0,\mathrm{r}} = \left(1-\sqrt{2q_2}\right)r_{\mathrm{CR}}. \quad (36)$$

From equation (35) the short axis of the inner R_1 ring is

$$64'' = r_{0,\mathrm{R_1}} = \left(1+\sqrt{2q_2}\right)r_{\mathrm{CR}}. \quad (37)$$

Adding these two equations, we obtain the corotational radius, $r_{\mathrm{CR}} = 52.''25$. This simple procedure can be carried out for any observed rotation curve via equation (34). Note that the galaxy must have both an inner ring and an outer R_1 ring for this procedure to be valid. Although there are many known examples of galaxies having both features (e.g., Buta & Crocker 1991; Buta 1995), most galaxies have either one or no ring (Buta & Combes 1996). The inclination of a galaxy may introduce error if it is significant and poorly known. The ratio of the maximum of the inner ring to the minimum of the outer R_1 ring is independent of the inclination of the galaxy. Then we use the values and equations above to estimate the perturbing potential. Substituting in equation (35), for the flat rotation curve of NGC 3081, $q_2 = 0.0322$, which agrees reasonably well with the 0.035 found from our *n*-body simulations, as described in later sections. Again, this can be carried out for any observed rotation curve.

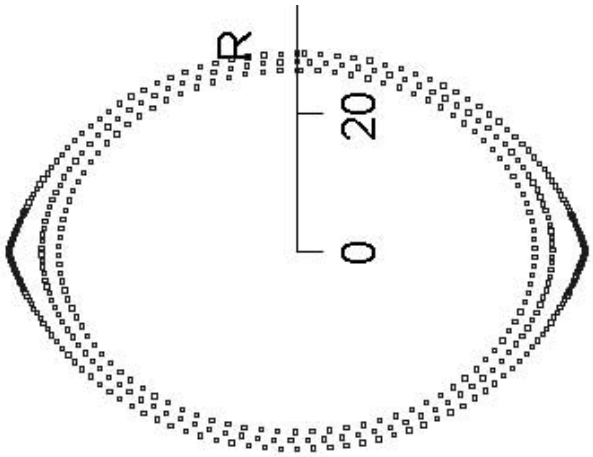

FIG. 8.—Analytic model of the r ring. CR = 54″; the flat rotation curve $m = 2$ bar potential perturbation is 0.023. Thus, the ring is a bit "fatter" than NGC 3081. Squares are plotted at equal intervals of time. Note the transverse crowding at the major axis, favoring the formation of associations there. Extreme crowding and slow motion relative to pattern speed occurs at the pointy ends, so that associations form and grow older there. At smaller radii, the extremely young associations should form near the major axis, then move to progressively larger CCW angles as they age.

Should an R_1 ring not be present, one can obtain the perturbation from the ratio of the minor and major axes of the inner ring alone. The semimajor axis of the inner ring is r_0. The minor axis is

$$r_{\mathrm{min}} = \left(1-\sqrt{4q_2}\right)r_0, \quad (38)$$

which is 24.″7 for $q = 0.0322$ found earlier. Using our *HST* observations, the observed semiminor axis of the outer edge is about 26.″5 (Paper I, Fig. 7). We see that

$$r_{\mathrm{min}}/r_{\mathrm{max}} = 1-\sqrt{4q_2}. \quad (39)$$

The ratio of the maximum and minimum distances for the inner ring provide a good estimate for q for any galaxy with an inner ring, as long as the inclination of the disk can be determined reasonably well.

The long R_1 dimension is given by equation (34) with $r_0 = 64''$, example potential, and $q = 0.0322$ so that

$$r_{\mathrm{R_1,max}} = r_{\mathrm{CR}}+r_{1,\mathrm{max}} = r_0+r_0 2\sqrt{q_m} = 86.''9, \quad (40)$$

which matches well the observed NGC 3081 outer ring maximum radius (85.″3; see Fig. 15 of Buta & Purcell 1998).

We have made an example plot, displayed in Figure 8, of the inner ring using the near-CR equations (30) and (34) with equation (22). The points are at equal time intervals. This figure displays well the qualitative features of the inner ring that are not present in the near-LR formulation of the inner ring (Fig. 7). As mentioned earlier, orbits inside CR are elongated along the bar inside and near to CR. Note how the smaller orbits inside r_0 are

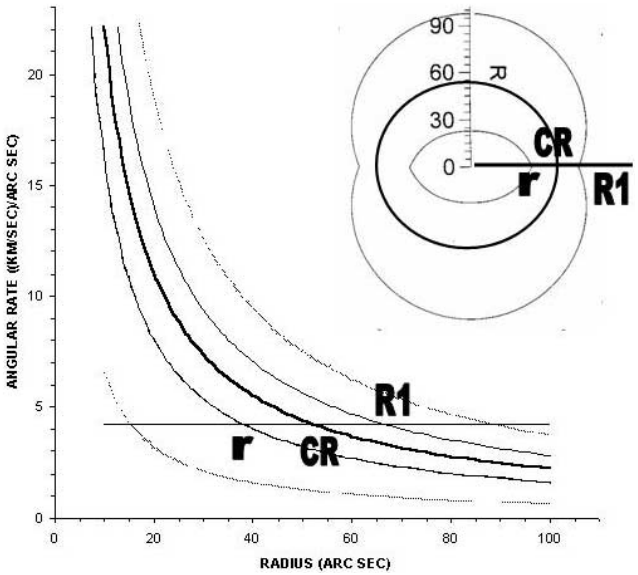

FIG. 9.—Angular rates vs. radius of NGC 3081 model. The heaviest line is the undisturbed 221 km s^{-1} flat rotation curve orbital angular rate, Ω_0. Using eq. (35) (example potential), the next heaviest lines beneath and above Ω_0 are the largest and smallest (respectively) circular r_0 radii for circulating particle perturbed CR solutions. The $m = 2$ perturbation potential $q = 0.0321$. The two lightest curves above and below the orbital rate line are the LR radii from eq. (10). The horizontal line is the pattern speed, $\Omega_p = 4.23$ km s^{-1} arcsec^{-1}. Intersections of the CR solutions with Ω_p give the largest r and smallest R_1 ring radii inside and outside the CR radius intersection. The smaller and larger radii of the intersections of the two lightest lines with the horizontal pattern speed line match the ILR and OLR radii, respectively. These two radii are somewhat larger and smaller than the largest nr and smallest R_2 ring radii, respectively. A schematic diagram of the rings and intersection points is also shown.

more circular. *This is observed in NGC 3081, where Buta & Purcell (1998) note that the eccentricity of the inner ring is larger as one gets closer to CR*. Because of the change from circular to elongated as CR is approached from smaller radii, there is orbit crowding in the radial direction near the minor axis. There is no radial orbit crowding near the major axis. However, note that there is considerable transverse crowding near the major axis. Plots of the R_1 formulation have "points" extending inward at the short axis along the bar.

In Figure 9 we display a summary of the above discussion. Angular rates are shown versus radius of the NGC 3081 model. The heaviest line is the undisturbed 221 km s^{-1} flat rotation curve orbital angular rate, Ω_0. According to equations (21) (general potential) and (35) (example potential), the next heaviest lines beneath and above Ω_0 are the largest and smallest (respectively) circular r_0 radii for circulating particle perturbed CR solutions. The $m = 2$ perturbation potential amplitude is qV_0, where $q = 0.0321$. The two lightest curves above and below the orbital rate line are the Lindblad resonance (LR) radii from equation (10). The horizontal line is the pattern speed $\Omega_p = 4.23$ km s^{-1} arcsec^{-1}. Intersections of CR solutions with Ω_p gives the largest inner ring and smallest outer R_1 ring radii inside and outside the CR radius Ω_0 intersection, respectively. The lightest lines match the inner and outer LRs whose intersections with Ω_p are somewhat larger and smaller than the longest nuclear ring and shortest outer R_2 ring radii, respectively. A schematic diagram of the rings and the inner ring, CR, and outer R_1 intersection points is also shown.

Overall, the beautiful ring pattern of NGC 3081 seems to be described well by this formulation. *Using the near-CR and LR equations, we thus see that q_2 appears to be a constant from the interior radius of the inner ring at* 34″ (6 kpc) *to the inner edge of the outer* R_1 *ring at* 85″ (15.0 kpc). For the outer R_2 ring, the OLR formulation discussed in the first part of this paper suffices. Figure 6 shows a nice agreement with the observed R_2 ring shape. A $q_2 = 0.035$ perturbation even suffices out to almost 100″ (18 kpc). Observationally, the R_2 ring is not so well defined, and the value of q_2 from 85″ to 100″ is less certain.

9. RING SHAPES AND BAR STRENGTH IN NGC 3081: CONSTANT VERSUS NONCONSTANT *M*/*L*

The quantification of bar strength in disk galaxies has seen some progress in recent years. Under the assumption of a constant stellar disk mass-to-light ratio (*M*/*L*), Buta & Block (2001; see also Buta et al. 2004b) used the maximum, Q_g, of the ratio of the transverse acceleration to the mean radial acceleration as a measure of the bar strength, following Combes & Sanders (1981). This is known as the gravitational torque method (GTM). The GTM uses the near-infrared surface brightness distribution to derive the gravitational potential, assuming a constant *M*/*L* over the disk (Quillen et al. 1994; Laurikainen & Salo 2002). In spiral galaxies, Q_g can be significantly affected by spiral arm torques (Buta et al. 2003). The constant *M*/*L* assumption is most likely valid in high-luminosity galaxies where the relative contribution of the dark matter halo is low (Persic et al. 1996; Buta et al. 2004b).

Our analytic analysis here allows us to estimate the bar strength in NGC 3081 in a completely different way: from the shapes of the rings. This is an approach that does not depend on assumptions concerning *M*/*L*. We multiply the right-hand side of equation (5b) by r_0 and substitute equation (29) to obtain mqV_0^2/r_0, and divide by the radial acceleration, V_0^2/r_0, obtaining

$$F_t/F_r = mq_m = 0.07. \quad (41)$$

This quantity is 0.07 from the minor axis distance of the inner ring to almost 85″, the major axis radius for the outer R_1 ring for NGC 3081. We cannot be sure beyond this, since the R_2 ring is not so clear as the other rings. The corotational resonance ring response is rather large even for the weak $q_2 = 0.033$ perturbation, so these rings should provide a good estimate of the bar strength.

This wide radial range of constant bar strength seems consistent with NGC 3081 having the full array of rings, even the two outer R_1 and R_2 ring types. However, it should be noted that in a typical barred galaxy, $|F_t/F_r|$, has a single maximum near the ends of the bar and declines smoothly from this maximum on either side (e.g., Buta et al. 2003; Block et al. 2004). In contrast, our estimate of the bar strength is made using dynamics from the ring shapes and rotation curve. In addition to the analytic estimate from the ring shape, we have verified the analytic formulation with simulations, as described later in this paper. We have carried out a calculation of F_t/F_r for NGC 3081 using the GTM, with a constant *M*/*L* assumed. The parameter rises to 0.2 at 32″, and then declines to 0.105 at 50″. These values are significantly different from 0.07 and are not constant. The different assumptions in the two approaches to bar strength are undoubtedly responsible for this disagreement; and we note that the GTM with constant *M*/*L* may not be justified for NGC 3081.

10. *IVB* PHASE ANGLE COLOR-AGE RELATION

If one examines equation (30) as a differential of the change in position angle in radians, then

$$d\phi_{1,\mathrm{pen}} = \pm \frac{V_0}{r_0} \sqrt{\left(\frac{r_{\mathrm{CR}} - r_0}{r_{\mathrm{CR}}} \right)^2 + 2q_m \cos 2(\phi_{1,\mathrm{pen}})}\, dt, \quad (42)$$

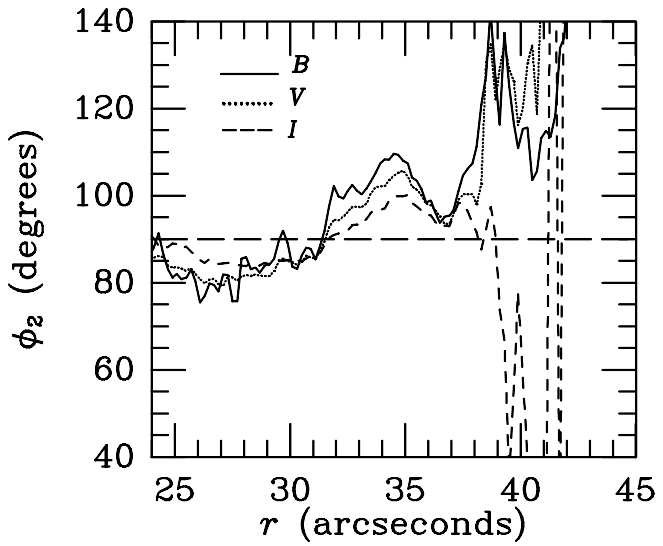

FIG. 10.—Fourier analysis around/along the ring. CCW angles from 90° to bar of $m = 2$ *IVB* color peaks over the 34″–37″ ring are plotted vs. radius. The bar is shown by the 90° line; *B* is plotted with a solid line, *V* with a dotted line, and *I* with a dashed line. Fourier amplitude shows smooth change over the 34″–37″ radius range with CCW separation of *I* and *B*.

where the minus sign is for points outside CR and the plus sign is for points inside. At r_0, one sees that there is no change in position angle for a given time interval. Then at radii smaller than r_0, the change in phase angle becomes larger.

Figure 10 shows a plot of the phase angles of the $m = 2$ maximum of the relative Fourier intensity component around the ring versus radius. This is an enlarged version of one of the panels of Figure 10 of Paper I. The peaks in the *I*, *V*, and *B* bands are shown. *Note that at r = 37″, the location of the exterior edge of the inner ring, all three bands coincide in their position angle.* We identify this "inner ring coincident radius" with the r_0 radius solution with equation (21a) or (30) set equal to zero for r_0 inside CR. At smaller r_0 than this, the equation (42) angle increments will be progressively larger positive quantities. This matches our expectation described above, with a clear larger separation at smaller distances with first *I*, then *V*, and finally *B*, in the direction of disk rotation. On the basis of the analysis in Paper I, the disk of NGC 3081 rotates counterclockwise on the sky. *The counterclockwise I, V, and B sequence thus appears to be a phase angle color-age sequence.* We expect that with deep enough observations we will see a reverse, clockwise *I*, *V*, *B* sequence outside the r_0 of the outer R_1 ring as the radius increases along the bar.

Note also that we expect that the 37″ inner ring color coincident radius (as defined above) is *not* the CR radius. Instead it is smaller, being close to the solution of equation (36) with the minus sign at $r_{0,r} = [1 - (2q_m)^{1/2}]r_{\rm CR} = 38\farcs5$, i.e., near the long dimension of the inner ring. If the observations become good enough, we predict that an outer ring color coincident radius will also be found at $r_{0,\rm R1} = [1 + (2q_m)^{1/2}]r_{\rm CR}$ or 64″ (12 kpc), the *short* dimension of the outer R_1 ring.

For the inner ring, as one goes inward from CR, the *IVB* color phase angles separate as discussed above. However, one will then approach from outside the ILR. As discussed earlier, the orbits near the ILR will be elongated along the major axis with positive $r_{1,\rm LR}$ amplitudes. Examining equation (7) with equation (28) substituted, one can see that the color phase angles will again get closer in angle as one goes to smaller radii. It should be emphasized that this is not a shifting of the peak of the emission in these bands from the major axis, but it is instead a greater asymmetry in the CCW direction of the *B* band compared to the *I* band, for example.

11. DISK SURFACE DENSITY

11.1. *Perturbations and Poisson's Equation*

The success of our match over a large range of radii argues that the perturbing potential we assumed is a realistic match. To calculate the total disk surface mass density perturbation as a function of radius using the bar strength, we use Poisson's equation (e.g., Mihalas & Routly 1968, p. 159) in cylindrical coordinates,

$$\frac{1}{r}\frac{\partial}{\partial r}\left(r\frac{\partial\Phi}{\partial r}\right)+\frac{1}{r^2}\frac{\partial^2\Phi}{\partial\phi^2}+\frac{\partial^2\Phi}{\partial z^2}=4\pi G\rho, \qquad (43)$$

where $\rho = \rho_0 + \rho_2$ is the axisymmetric plus perturbation volume densities. Equation (4) gives the potential in the middle of the disk plane. The axisymmetric potential component, Φ_0, satisfies Poisson's equation with ρ_0 on the right-hand side. We can thus subtract these out, leaving only the perturbation terms. The cosine function appears in all terms of Poisson's equation and is divided out.

We integrate over z from $-\delta$ to δ, encompassing several times the exponential scale height of the disk, so that the right-hand side becomes a function of the surface density amplitude $4\pi G\mu^A_{d,2}$. In observations of edge-on disk galaxies and the Milky Way, the exponential scale height h_z is typically 0.35 ± 0.1 kpc and is nearly constant with radius (Gilmore et al. 1990, p. 218; see also de Grijs 1998). For the portion of the disk we are studying, δ should thus be small compared to the r_0 of the inner ring, 7 kpc, as we assume henceforth. We want to calculate the surface mass density perturbation for $m = 2$,

$$\mu_{d,2} = \mu^A_{d,2}\cos\left[2(\Omega-\Omega_p)t\right]. \qquad (44)$$

The first and second terms of the left-hand side are continuous even functions of z across the disk plane. The integral of the factor dependent on z for both of these terms is thus zero across the disk plane. The contributions to the integral at equal distances above and below the plane cancel one another.

Now we evaluate the third term on the left. Since the integral of the second derivative is the first derivative with respect to z, the third term on the left-hand side becomes

$$\left.\frac{\partial\Phi^A_{p,2}}{\partial z}\right|_{-\delta}^{+\delta} = 2\left.\frac{\partial\Phi^A_{p,2}}{\partial z}\right|_{z=\delta} = 2(2\pi\mu^A_{d,2}). \qquad (45)$$

Here we evaluate the inner ring size for a point on the bar axis 7 kpc from the center. The factor in parentheses on the right hand side is merely 2 times the potential gradient above a uniform thin sheet of uniform density ($\mu^A_{d,2}$) obtained by direct integration of the gravitational force law (e.g., Mihalis & Routly 1968, p. 188). In this integration, at a point a distance δ from the disk, practically all the acceleration contribution comes from points within, say, 5δ. With a disk scale height of 0.35 kpc as previously assumed, we see that equation (45) is a good approximation for finding the amplitude of the azimuthal density variation at the 6.93 kpc radius end of the major axis of the ring. Thus, for a bar with $m = 2$ and a small distance $\delta \gg r_0$ from the disk plane, we can assume a perturbing potential amplitude in equation (4) of

$$\Phi^A_{p,2} \approx -q_2 V_0^2 e^{-|z|/r_0}. \qquad (46)$$

TABLE 1

I_2/I_0 AT DIFFERENT DISTANCES FROM THE CENTER OF NGC 3081

Radius	I_2/I_0	$\mu_{d,0}$ ($M_\odot$ pc^{-2})	$\mu_{M,100\%}/\mu_{d,0}$	I_0 ($L_{\odot,H}$ pc^{-2})	M/L ($M_\odot$ $L_{\odot,H}^{-1}$)
40″ (7.20 kpc).....	0.68	12.8	19.4	122.8	0.104
50″ (9.00 kpc).....	0.59	11.8	16.9	47.4	0.249
70″ (12.6 kpc).....	0.25	19.4	7.14	21.28	0.912

NOTE.—Columns show disk surface densities, "halo/disk" parameter ($\mu_{\mathrm{M},100\%}/\mu_{d,0}$), and mass-to-light ratio (M/L) in solar units.

For $m = 2$, this potential produces (1) the uniform sheet force law at small distances $|z| \gg r_0$ from the disk (e.g., Mihalis & Routley 1968), (2) the boundary condition potential value in the middle of the disk plane, and (3) the boundary condition approach to zero at infinity. For radii that are not large compared to the disk thickness, this approximation will be less valid, and the magnitude decrease with increasing distance z will be faster. Here we have used an approach very similar to that in BT for stability of a shearing sheet. Substituting equation (46) into Poisson's equation (45), we can solve for the surface density amplitude for our perturbation of the example potential,

$$\mu_{d,2}^{A} = \frac{q_2 V_0^2}{2\pi G r_0}. \tag{47}$$

We want to obtain the unperturbed or azimuthally averaged disk surface density, $\mu_{d,0}$. As mentioned before, in the usual procedures for obtaining this quantity (Quillen et al. 1994), a diskwide mass-to-light ratio (M/L) is assumed and the near-infrared light distribution is used to obtain surface densities. These surface mass densities, including thickness, then give the bar strengths as calculated by Buta & Block (2001). Because of the result we have obtained above, we do not need the constant M/L ratio assumption. We can use the ratio of the near-infrared, $m = 2$ Fourier surface brightness component to the circularly symmetric $m = 0$ component, $I_2/I_0 = \mu_{d,2}^{A}/\mu_{d,0}$, *at the radius of the inner ring*. We do *not* assume a diskwide M/L ratio or any value of the ratio at all. Instead, we only assume that the local disk surface brightness perturbation ratio is proportional to the surface mass density perturbation ratio at that radius. We thus obtain a local mass density *at that radius*. This is a total surface mass density of material in the disk but not in the high-dispersion halo.

Using this assumption and the equation for the surface density perturbation given above, we obtain an equation for the total disk surface density of a resonance ring galaxy like NGC 3081,

$$\mu_{d,0} = q_2 \frac{V_0^2/2\pi G r_0}{I_2/I_0} = \frac{q_2 \mu_{\mathrm{M},100\%}}{I_2/I_0}, \tag{48}$$

where $\mu_{\mathrm{M},100\%}$ is the surface density of an imaginary thin Mestel (1963) disk, $V_0^2/(2\pi G r_0)$, which would generate a flat 221 km s^{-1} rotation curve like that of NGC 3081.

11.2. *Calculating the Disk Surface Mass Density of NGC 3081*

In a Fourier analysis of the observed NGC 3081 disk, at the radius of the inner ring, the ratio of the H band (1.65 μm) intensity components $I_{m=2}/I_{m=0}$ has been obtained and used by Buta & Purcell (1998). A plot of this ratio versus radius for NGC 3081 is shown in Figure 5. Values of the intensity ratio are given in Table 1. We here give the details of the calculation for one radial distance, 40″ or 7.2 kpc, at which $I_2/I_0 = 0.68$.

For the inner ring through outer ring radius range, we have estimated the perturbation potential to be a constant, $q_2 V_0^2 = 0.035 V_0^2$, using the ring shapes so that equation (48) should be valid. Given a circular velocity of $V_0 = 221$ km s^{-1}, CR at 54″ or 9.72 kpc radius, and a semimajor axis of the deprojected inner ring of about 40″, a radius of 7.2 kpc, then $\mu_{\mathrm{M},100\%} = 250\ M_\odot$ pc^{-2} at 7.2 kpc. NGC 3081 has practically no classical bulge.

We can now substitute in equation (48) to obtain $\mu_{d,0} = 0.0515\mu_{\mathrm{M},100\%} = 12.8\ M_\odot$ pc^{-2}. This value at 7.2 kpc radius in NGC 3081 is smaller than the local disk surface density found in our Galaxy by about a factor of 4. We see that the NGC 3081 stellar surface density at 7.2 kpc is 0.0515 times the density $\mu_{\mathrm{M},100\%}$ of a 100% Mestel (1963) disk that will produce a $V_0 = 221$ km s^{-1} flat rotation curve like that seen in NGC 3081. This corresponds to a ratio of the pure Mestel disk to the actual surface densities as the measure for all components of NGC 3081 to its self-gravitating disk alone, $\mu_{\mathrm{M},100\%}/\mu_{d,0} = 19.4$. We thus see that at 7.2 kpc, the dynamics of NGC 3081 is dominated by an inert "halo" component rather than by the disk itself.

Table 1 shows values at larger distances than the 7.2 kpc 12.8 $M_\odot$ pc^{-2}. The surface mass density at 9 kpc and surface density ratio is a bit smaller, 11.8 $M_\odot$ pc^{-2}. Farther out, at 70″ (17 kpc), the disk surface density is larger (24 $M_\odot$ pc^{-2}) and the ratio of the maximum 100% disk to the disk is a good deal smaller ($\mu_{\mathrm{M},100\%}/\mu_{d,0} = 7$). However, the dynamics of NGC 3081 is still halo-dominated at this radius. The existence of the orderly set of rings over a large distance range may be an indication of the halo domination. This is certainly the case in our simulations as we will discuss later.

Comparing to the Milky Way Galaxy in the solar neighborhood, the most recent estimate using *Hipparcos* data is $56 \pm 6\ M_\odot$ pc^{-2} (Holmberg & Flynn 2004). The estimate for visible matter is 53 $M_\odot$ pc^{-2}. Thus, there is little evidence for dark matter within the local disk. Taking the circular velocity in the solar neighborhood to be $V_0 = 221$ km s^{-1} and the Sun to be 8 kpc from the center, the Mestel 100% surface density is 225 $M_\odot$ pc^{-2}. The ratio $\mu_{\mathrm{M},100\%}/\mu_{d,0} \approx 4$ for the solar neighborhood. The Sun's location is the best galaxy location for which all the information necessary to estimate disk surface density, disk scale height, and velocity dispersion is available.

How good is our surface density estimate method compared to other methods for external galaxies? Other methods require measurement of the disk vertical velocity dispersion and the scale height at each location in the disk (see, e.g., Gilmore et al. 1990, p. 216). The surface density is roughly proportional to the velocity dispersion squared divided by the scale height. For external galaxies, it is hard to determine both of these quantities for the same galaxy with any accuracy. One can best be measured when the galaxy is face-on, the other when edge-on. For our calculation, we do not require measurement of the velocity dispersion and require only that the scale height be small compared to the radius at which the calculation is made.

11.3. *Isophote Method Proposed by Contopoulos and the Shapes of Resonance Rings*

Is the above surface density calculation method reasonable? We are reassured that Contopoulos (1979) suggested something similar. Contopoulos noted that well away from resonances, the equation for the deviation of a periodic orbit from a circle can be set in the self-consistency equation, where the density perturbation is derived from the perturbation potential by Poisson's equation. Contopoulos suggested that stellar disk isophotes of barred galaxies could be used to obtain the pattern speed and the magnitude of the bar potential perturbation as a function of radius. The tilt of the galaxy must be known and its effects removed in this procedure. Our procedure is in principle similar, except that we use the resonance rings rather than stellar isophotes to obtain the perturbation potential. In contrast to isophotes, the rings can clearly be identified with particular periodic orbits. Because they are close to resonances, the rings show large deviations from circularity, so that their shapes and size ratios are insensitive to and even independent of moderate tilts of the galaxy disk. We have attempted to use the outermost isophotes of NGC 3081 in a surface density calculation, and find that their shape is sensitive to the particular value of the inclination assumed as well as to the perturbation.

Buta (2002) has shown that the deprojected inner ring shape in a small sample of early-type spirals correlates only weakly with GTM bar strength Q_g. It is possible for two galaxies to have the same apparent bar strength and very different intrinsic ring shape. Buta (2002) showed that nearly circular rings can be found at almost any bar strength, while highly elliptical rings are found mainly for relatively strong bars.

If the circular rings are also the periodic orbits we have discussed, we would estimate q_2 to be small. This would then lead to a small surface mass density for these galaxies (via eq. [48]). In our simulations, after the bar perturbation is introduced but before a clear periodic orbit inner ring forms, we see no temporary round rings but instead distorted spiral features with elongated shapes resembling the long and short dimensions of the final inner ring, whose elongation is a function of the strength of the bar perturbation. This is consistent with the more extensive simulation survey of Byrd et al. (1994), who find that "As the bar is weakened, the inner ring becomes more circular." This was confirmed by Salo et al. (1999). Nevertheless, the wide range of ring shapes at significant bar strength indicates that other factors are involved in determining some ring shapes. Interestingly, Buta (2002) found that when his sample is restricted to galaxies having R_1 outer rings or pseudorings, a correlation between intrinsic inner ring shape and bar strength is found, with stronger bars having more elongated inner rings. The presence of an R_1 ring could therefore indicate that periodic orbits more accurately reflect the strength of the bar.

12. DISK MASS-TO-LIGHT RATIO (M/L)

12.1. *Surface Brightness as a Function of Radius*

Note that our method and that of Contopoulos makes no assumptions about the mass-to-light ratio (M/L) for the disk, in contrast to other methods for estimating disk surface density (e.g., Quillen et al. 1994; Quillen & Frogel 1997). We can thus obtain M/L as a function of radius using our surface mass density results and the observed surface brightness. The surface brightness of the outer H-band disk of NGC 3081 can be expressed as

$$I = I_0 e^{-r_0/s}, \tag{49}$$

where s is the radial scale length. The observations are shown in Figure 6. To obtain the parameters for this formula, we convert the surface brightness in mag arcsec^{-2} to $L_{\odot,H}$ arcsec^{-2} then to $L_{\odot,H}$ pc^{-2}. According to Buta & Purcell (1998), at 100″, the disk surface brightness of NGC 3081 is $\mu_s = 23$ mag arcsec^{-2} in the H band. The Sun's absolute H magnitude is 3.37 (Worthey 1994); the Sun's apparent magnitude at 32.5 Mpc is 36.0. Thus, 1 arcsec^2 is 13 H mag brighter than the Sun, or 1.59×10^5 $L_{\odot,H}$ arcsec^{-2}. Using the 158 pc to 1″ factor, we obtain 6.31 $L_{\odot,H}$ pc^{-2}. Using this value with the exponential scale length, s, of 25″ or 15.7/4 kpc, the constant $I_0 = 350$ $L_{\odot,H}$ pc^{-2}.

12.2. *The Disk M/L of NGC 3081*

The M/L of NGC 3081 is given by the surface mass density divided by the exponentially declining surface brightness. We choose the H band to represent the majority old stellar disk population. From equation (49), at 40″ the exponential surface brightness is 70.66 $L_{\odot,H}$ pc^{-2}. However, the 40″ and the inner ring are within the "lens," so that the surface brightness is higher than the exponential by about 0.6 mag. This lens is clear in Figure 6. The surface brightness is, consequentially, $70.66 \times 1.7378 = 122.8$ $L_{\odot,H}$ pc^{-2}. At 40″ we thus obtain $M/L = 12.8/122.8 = 0.104$ $M_\odot$ $L^{-1}_{\odot,H}$. The last column of Table 1 gives the M/L values for 50″ and 70″. We see that there is a trend from the small value at 40″ to the largest value of 0.912 at 70″.

We can use the M/L to judge how recently the stars in the outer stellar disk formed or whether dark matter is found in the disk. A ratio of $M/L = 1.19$ $M_\odot$ $L^{-1}_{\odot,H}$ is the value calculated by Worthey (1994) for a 12 Gyr old [Fe/H] = 0 population. We see that there is a lower M/L at smaller radii. We thus see no evidence for dark matter in our disk at 70″. Unfortunately, the data in Figures 5 and 6 are not good enough for us to calculate values at 80″ or beyond. The results show that the assumption of a diskwide constant M/L may not be valid for NGC 3081. The M/L variation with radius is a factor of almost 9 in NGC 3081 from 40″ through 70″.

13. RING STAR FORMATION: OBSERVATIONS VERSUS THEORY

The distribution of point sources, Hα emission, and a reddening-free photometric parameter (Q_4) versus position angle are shown in Figure 4. In this plot,

$$Q_4 = (U - B) - 0.32(B - I) \tag{50}$$

is more negative for younger association ages. The Hα data are from Buta & Purcell (1998) and are in arbitrary flux units. Stronger Hα corresponds to a young association age, weaker Hα to an older association age. In Figure 4, we divide the associations into two age groups by Hα. This division agrees with the Q_4 age parameter, with the high Hα emission group having a more negative average of -0.889, and the lower Hα having a less negative average of -0.760. Looking at the younger (*upper*) and older (*lower*) plots, one sees an asymmetry in the distribution in a CCW sense with young associations (Hα flux > 100 and $Q_4 = -0.9$) appearing near the bar in disk plane position angle at 0° and 180°. However, most of the lower graph's older associations appear immediately after the 0° and 180° position angles of the bar, not immediately before or with symmetry. This is a CCW asymmetry. Even in the ground-based color observations (Buta & Purcell 1998), there is a clear color asymmetry across the end of the bar, with bluer colors occurring after the bar in position angle, as do the Hα flux > 100 and $Q_4 = -0.9$ associations.

We thus verify the qualitative color sequence of a long-wavelength peak and star formation peak near the bar ends, followed by the "lighting up" and increasing age of the young associations along the direction of orbital motion relative to the bar. Inside CR, for the exterior edge of the ring, this will be faster than the bar. Outside CR, there is a reverse CW asymmetry, as can be clearly seen in the Hα display of the outer ring of NGC 3081 in Buta & Purcell (1998). This sequence and the CCW/CW inversion NGC 3081 provides a clear time sequence "laboratory" of star formation.

14. AMPLIFICATION, SELF-GRAVITY, AND VELOCITY DISPERSION

14.1. *Reduction Factor, Force Softening, and Disk Velocity Dispersion*

We have shown that there is some radial crowding at the minor axis and strong azimuthal crowding at the major axis crossings of the ring. However, we need to ascertain the effect of self-gravity in star formation around the ring. Star-forming regions are less numerous near the minor axis. Instead, the young associations are mainly distributed within $\pm 60^\circ$ of the major axis crossing, around the bar ends (see Fig. 11 of Paper I). We want to clarify why the star formation is weak near the ring minor axis, strong near the major axis, and why it spans such a wide angular range around the bar ends. We shall see that this range is the result of the process of gravitational amplification leading to star formation. We use as references Byrd (1995) and Toomre (1981).

We introduce m as the perturbation multiplicity, here equal to 2. The angle between the outward trailing arm and the radial line is γ. We should note that observers typically use arm pitch, cot i, where $i = 90^\circ - \gamma$. The arm pitch is the angle between the outward trailing arm and a circle through the arm.

The dynamics of the disk are dominated by a stellar component with a velocity dispersion σ, which can reduce the effect of self-gravity. The "reduction factor," $\mathcal{F}$, specifies how much the self-gravitational response to a perturbation is reduced below the $\mathcal{F} = 1$ of a disk with no velocity dispersion. Toomre (1981) uses the complicated "hot stars" reduction factor derived by Lin & Shu (1966) and by Kalnajs (1965) as the most realistic. Compared to the complicated hot stars reduction factor, BT state that the softened gravity formulation developed by Miller (1971, 1974) "provides close analogs to stellar disks. . .that. . .are much easier to investigate numerically." Athanassoula (1984) has a very complete discussion of this question. Softened gravity is also very convenient analytically. We therefore deviate from Toomre's theoretical discussion by using the softened gravity reduction factor,

$$\mathcal{F} = e^{-ka} = e^{-[m/(r\cos\gamma)]a}. \tag{51}$$

One can think of a as behaving like a Jeans length for both stars and gas, due to the velocity dispersion of the stars or gas clouds. Although the discussion is appropriate for stars or gas, we are more interested here in the gas clouds' disk. The gas clouds' disk thickness a is related to the disk surface density, μ, and the gas clouds' vertical velocity dispersion, σ_z, as (van der Kruit 1988; also in Gilmore et al. 1990)

$$\sigma_z = \sqrt{(\pi^2/2)G\mu a} \tag{52}$$

for the velocity dispersion in the disk plane. The exact parenthetical value in equation (52) does not strongly affect σ because of the square root. In our case we are interested in the gas clouds. Because gas cloud masses are large compared to those of individual stars, $a_{\rm gas}$ will be smaller than $a_{\rm stars}$ because of the clouds' low dispersion velocities. However, the surface mass density of the gas component will be much less than the stellar disk surface density; probably so low that, undisturbed, it too would be stable against growth of all m features in an unperturbed disk.

14.2. *Stability Parameter and Star Formation*

Examining the analytic plot of the "near-CR" inner ring given earlier, in terms of the amount of surface density enhancement the minor axis is not a favorable position for association and star formation. In terms of density enhancement and transverse collisions, the major axis points are best suited to stellar association formation. At the tips, the azimuthal crowding is very large. The existence of disk self-gravity will extend the angular range of star formation around the ring ahead and behind the major axis points, as we observe.

For our best fits to the inner ring, i ranges from $\pm 31^\circ$ near the major axis to 0° at the minor axis. We can thus follow Toomre's (1981) approximation, $\cot i = 1/\cos\gamma$. Going from the major axis toward the minor axis, $\cot i$ increases. As $\cot i$ increases, we have more gravitational amplification. The velocity dispersion, σ_z, can rescue the disk material from instability. Solving for the minimum needed softening, a, or equivalently the minimum needed velocity dispersion, σ_z, Byrd (1995) obtained

$$Q_{Az} = \kappa\sqrt{\frac{ae}{2\pi G\mu_{d,0}}} = \left(\sqrt{\frac{2ea}{r_0}\frac{\mu_{\rm M,100\%}}{\mu_{d,0}}}\right)_{\rm M} = \frac{\kappa\sigma_z}{3.38G} = \frac{\mu_{\rm M,100\%}}{\mu_{d,0}}\left(\frac{2\sqrt{e}}{V_0}\right)_{\rm M}\sigma_z, \tag{53}$$

where we use the equation (52) conversion. The terms or factors in the equations above pertaining to a flat rotation curve Mestel disk are indicated by the subscript M. If Q_{Az} is unity, the undisturbed disk is stable, with no clumps developing. Equation (53) is the same as that obtained using exponential softening to study *axisymmetric* stability (e.g., as done in BT). The reader will note that equation (53) is quite close to the standard Toomre Q_T stability criterion.

We use Q_{Az} rather than Q_T because the familiar Toomre stability parameter is for a growth of a circular ring, but the Q_{Az} is for growth of azimuthal lumps of various pitches as they wind up. In the NGC 3081 inner ring the pitch ranges from $i \approx 31^\circ$ near the tips of the ring to $i = 0^\circ$ at the minor axis. Byrd (1995) also obtained the arm pitch, cot i, where amplification is greatest. Here all the parameters are defined as before, except we introduce the variable f, defined as $\mu_{\rm M,100\%}/\mu_{d,0} = (1 + f)_{\rm M}$;

$$\cot i_{\rm max} = \frac{\kappa^2 er}{2\pi G\mu_{d,0}mQ_{Az}^2} = \left(\frac{2e}{mQ_{Az}^2}\right)_{\rm M}\frac{\mu_{\rm M,100\%}}{\mu_{d,0}} = \left(\frac{2e}{mQ_{Az}^2}\right)_{\rm M}(1+f)_{\rm M}. \tag{54}$$

15. EXAMPLE POTENTIAL SIMULATIONS

15.1. *Simulation versus Analytic Results for Gas Disk Surface Density*

We now approach star formation in the inner ring of NGC 3081 using n-body simulations. We verify the findings from analytic theory. In addition to the stated approximations needed for analytic theory, n-body simulations have a variety of usually unstated deficiencies (e.g., Byrd 1995). We use the two approaches in a complementary fashion.

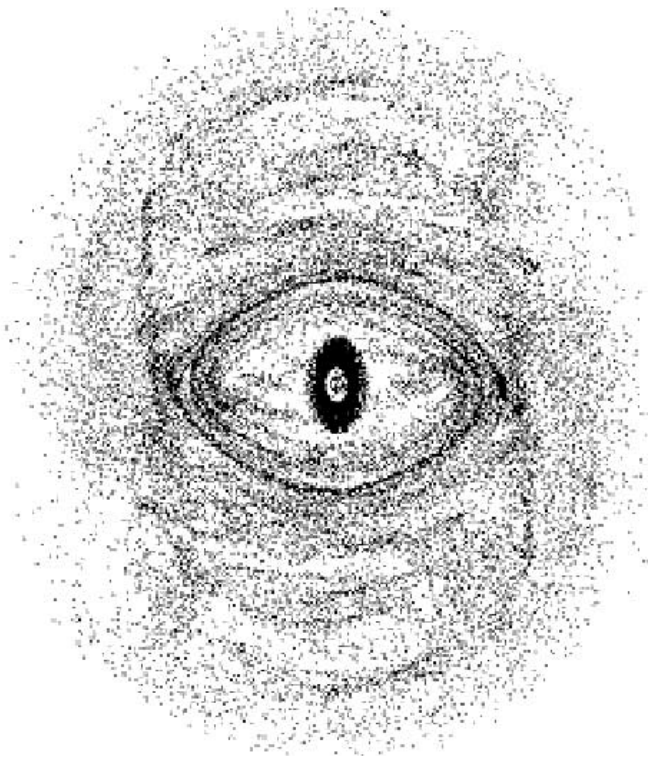

FIG. 11.—*N*-body gas cloud disk simulation about 4×10^9 yr after the onset of bar perturbation. Comparing to Fig. 1, note nr, r, and R_1 rings. The disk *gas cloud* surface density is 1/15 what is needed to create the flat rotation curve (halo-dominated). Clumps (associations) form near the analytically predicted pointy ends of the rings, as predicted. At lower gas cloud surface densities, the clumps do not form (as expected for the program "softening").

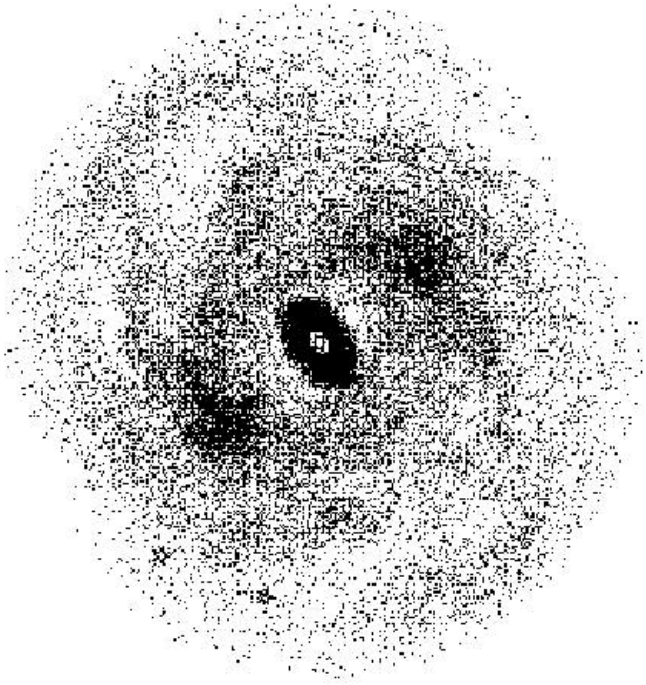

FIG. 12.—*N*-body gas cloud disk simulation about 4×10^9 yr after the onset of bar perturbation. The disk gas cloud surface density is 1/5.6 what is needed to create the flat rotation curve (halo-dominated). Clumps (associations) form around the ring and at the ring ends. These scatter other cloud particles and have few body encounters with each other that might destroy the ring. We emphasize that inelastic passages occur in this simulation, just as in the 1/15 simulation shown earlier. The small stars are just marker particles used to track orbital motion in the simulation.

The code used here is described in Howard et al. (1993), and discussed in more detail in the Appendix. We insert an unchanging, rotating bar perturbing potential in a two-dimensional stellar disk, like the "example" potential used in the analytic derivations. The stellar disk and halo are fixed, resulting in a constant V_0. We use 60,000 "gas clouds" in the simulations, which interact gravitationally. The gas clouds in the disk have an additional dissipative force on them in that, during each time step, they interact with neighboring clouds, with the resulting motion being the average velocity of the cloud and all its neighbors. We varied q_2 in the stellar disk bar perturbation potential given by equation (28). Figure 11 shows a dissipative gas cloud *n*-body simulation, which forms the inner ring nicely. Note the transverse crowding at the pointed ends, just as in the analytic Figure 8. Here $q_{\rm total} = 0.035$, with $q_2 \sim 0.033$ and a small $q_4 \sim 0.002$.

For the case of NGC 3081's ring, our best fit near the ends of the elongated inner ring is $i \approx \pm 31^\circ$. At the minor axis points, $i = 0^\circ$. We know that young associations form near the ends of the elongated inner ring. Taking the disk of gas clouds to be stable without the bar perturbation ($Q_{Az} = 1$), equation (54) gives a relation between the i of maximum star formation around the ring and the disk surface density, and the azimuthal spacing (size) of the associations that form. We see that at the minor axes, $i = 0^\circ$, so that the left-hand side is so large that the only m solution possible is zero, i.e., associations do not form. Near the ends of the analytic plots of the ring and the actual observed ring, $i = 31^\circ$ near the ring tips. If we evaluate equation (54) using $i = 31^\circ$, $m = 36$, and a Mestel disk, we find that associations should form in our simulations if $f \leq 10$. The $m = 36$ corresponds to the smallest 10° bin angular resolution of the simulation.

We have carried out simulations with various gas disk surface densities in a Mestel disk. We find that clumps start to form when $f \leq 15$, as shown in Figure 11. Considering the inelastic encounters of the gas clouds and collisions at the points of the inner ring, the larger value of f in the simulations is reasonable. Note that these results are for the disk gas component, not the stellar component. We thus estimate that the disk gas clouds in NGC 3081 make up $1/(1 + 15) = 1/16$ of the "100% disk" surface density as a crude lower limit.

15.2. *Ring Lifetime, Formation of Associations, and Disk Surface Density*

Because of the quality of the *HST* observations, we have evidence from individual associations for an estimate for the age of the inner ring. Analysis of the cluster colors in Paper I indicate that most of the brighter associations are 10 Myr or less in age. The Q_4 reddening-free index used in Figure 4, combined with model colors from Bruzual & Charlot (1996), suggest some ages up to 400 Myr for some clusters. Because clusters get less luminous with great age, this estimate must be considered a lower limit. We can investigate the ring lifetime with simulations. It should be emphasized that the program only starts with a set of gas clouds that can collide inelastically. The age of the associations identified in our *HST* observations indicates that continual formation of new clouds, along with destruction of the old, must occur to create the range of association ages observed. This simulation used 50 steps per crossing time for the disk. We take the NGC 3081 disk radius to be about 100″, or 18 kpc. The ring occupies about the inner third of the simulation disk, or 6 kpc. The crossing time is about 18 kpc/221 km s^{-1}, or 100 million years. Each time step is thus about 2 million years. The simulation shown

has preserved the ring for 1200 time steps, or about 2.4 billion years. There is thus no dynamical problem with the existence of associations over 400 million years old. However, complications like feedback may invalidate our age estimate, and our simulations have many approximations and ignore the effects of star formation on the rings. At best, one can say the age is probably between the 400 million year estimated age of the oldest associations and the couple of billion years in which the inner ring survives in the simplified environment of the simulations.

If we have too little halo, clumps quickly form, but some of them are very massive. Violent two-body encounters occur and the simulations end up with a big mess of scattered former association stars and no definite ring. A simulation with too little halo is shown in Figure 12. For the Figure 12 simulation, $\mu_{d,0}/\mu_{\mathrm{M},100\%} = 1/(1 + 5.6) = 1/6.6$ of a disk, totally sufficient to explain the rotation curve. This is a crude upper limit to the disk gas surface density, so it is probably comparable to 1/16 but certainly less than 1/7. There is clearly a best choice for the surface density of the gas cloud disk to gravitationally form associations in the ring.

16. CONCLUSIONS

We complement our *HST* observational study of the inner ring of the weakly barred early-type spiral galaxy NGC 3081 (Paper I) using a perturbative analytical approach and *n*-body simulations. We obtain a better understanding of the ring dynamics and a way to estimate the bar strength and disk surface mass density near the rings. We find that the misalignment of the major axis of the nuclear ring with respect to the bar could be due to significant dissipation in the gas clouds making up the ring. We obtain the misalignment in both our analytic formulation and our simulations, both with dissipation. We find that a gas cloud inner ring forms under a rotating bar perturbation with very strong azimuthal cloud surface density enhancement at the two points where the ring crosses the major axis of the bar.

These enhancements, and a transition from a leading to trailing orientation as the orbiting clouds cross the major axis, explain the enhanced star formation ahead of and beyond the major axis crossing points. These luminous young associations thus outline the ring as they move around it in the circulating orbit possible at that distance from corotation (CR). At slightly smaller radii there is no enhancement, no luminous associations, and thus no delineation of a ring. A similar delineation can happen inside the Linblad resonance (LR) and more weakly outside the outer Lindblad resonance (OLR). The NGC 3081 disk turns counterclockwise on the sky, consistent with the sense implied by the dust distribution and radial velocities, and the same as the bar pattern speed. We explain the observed counterclockwise angular *IVB* color sequence as being due to the increasing age of stellar associations away from the ring major axis inside the exterior edge. The outer edge of the ring, where it crosses the bar major axis, has no expected or observed angular displacement between the *I*, *V*, and *B* Fourier components around the ring. The perturbed orbital angular rate is equal to the pattern speed at those two points. This is supported by the wide range of individual association ages deduced from our *HST* images at these two points. At smaller distances, as one crosses the ring, the *IVB* component displacement increases until the interior edge of the ring is reached.

We obtain a relation between the potential perturbation and the difference between the exterior edge of the inner ring and the interior edge of the outer R_1 ring along the major axis of the inner ring. We show how the potential perturbation strength can also be estimated from the inner and outer ring shapes and sizes. Figure 9 serves as a summary of these results for our model of the rotation curve, perturbation, and pattern speed values.

We show how the potential perturbation and the fractional long-wavelength twofold surface brightness variation can be used to calculate an unperturbed total (mostly stellar) disk surface density as a function of radius. We estimate 13 $M_\odot$ pc^{-2} near the NGC 3081 inner ring at 7.2 kpc, about 1/19 that of a 100% Mestel stellar disk sufficient to explain the observed 221 km s^{-1} flat rotation curve. This indicates that the galaxy is halo-dominated. Farther out (17 kpc), the surface density is significantly larger (23 $M_\odot$ pc^{-2}), with the halo somewhat less important (1/7).

The increase in disk surface density of NGC 3081 as one goes outward from the inner ring seems counterintuitive. However, one should note that the counterintuitive lower values occur in the neighborhood of the inner ring. Since we have evidence that the ring may be as much as a billion years old, it is not unreasonable that the massive cloud complexes (proto-associations) that form at the ends of the major axis would be very effective at scattering disk stars either inward or outward in a fashion qualitatively similar to the scattering of stars by clouds in our Galaxy. Better data for NGC 3081 and data for other galaxies will be useful in assessing whether disk modification by rings is important in other galaxies. It has been proposed that central black holes may have secular effects on their bars and disks. We see evidence here that a long-lived inner ring created by a bar perturbation may have an effect on the surface density of the underlying stellar disk of a galaxy.

It is usually assumed that the *M*/*L* ratio is constant over the disk in calculating disk and bar potentials. Buta et al. (2004b) discuss how this may be justified in high-luminosity galaxies. The surface mass density we obtain in equation (48) is for matter in the disk obtained with no assumption as to *M*/*L* ratio. When we divide by the disk surface luminosity, we obtain a disk *M*/*L* exclusive of any halo material in the neighborhood. Contrary to the usual assumption, for NGC 3081 our surface mass density estimates indicate that the *M*/*L* ratio of the disk is definitely not constant with respect to radius; we see a significantly smaller *M*/*L* ratio in the neighborhood of the inner ring. We need to apply this method to other resonance ring galaxies and also improve our data for NGC 3081 to see whether significant *M*/*L* variation with radius occurs in other galaxies. Even the largest *M*/*L* ratio we obtain for the outer ring region is consistent with a population of stars as old as the universe, the largest reasonable value for the old stellar disk. If we had obtained a much larger value, this would be evidence for dark matter in the disk of NGC 3081. We thus see no clear evidence of disk dark matter in NGC 3081. Better data like those shown in Figures 5 and 6, extending to 100″, and better determination of the shape of the R_2 ring will be needed to confirm whether the increasing *M*/*L* trend with radius as seen in the last column of Table 1 continues. If so, then there would be evidence for dark matter in the outer disk of NGC 3081. On the other hand, over the range of the resonance rings, the calculated surface density of the visible disk of NGC 3081 is quite insufficient to explain its rotation curve. We thus find evidence for a dominating halo in NGC 3081.

The ring lifetime of several billion years in our simulations is consistent with our *HST* observations that some associations are over 400 million years old, particularly near the ends of the ring major axis. We emphasize that these are merely order-of-magnitude estimates. With a sufficiently high gas cloud disk surface density, our simulations form gas cloud "associations" near the ends of the bar, as observed and expected. Too high a gas cloud surface density results in a chaotic nonring disk.

This work was supported by NASA/STScI GO grant 8707 to the University of Alabama and NSF grant AST 02-0177 to Bevill State College in Fayette, Alabama. R. B. also acknowledges the support of NSF grant AST 02-05143 to the University of Alabama.

APPENDIX

SIMULATION DESCRIPTION

The original version of this code was written by Miller (1968, 1970, 1974). Byrd et al. (1984) added the option of an orbiting perturber. Byrd et al. (1986) specified the two-dimensional potential as that of a finite Mestel disk (Lynden-Bell & Pineault 1978) of radius $R_{\rm M}$ and circular orbital speed, V_0,

$$\Phi(r) = \begin{cases} V_0^2 \ln \dfrac{r}{R_{\rm M}} & \text{for } r < R_{\rm M}, \\ -\dfrac{2V_0^2}{\pi} \displaystyle\sum_{l=0}^{l=5} \dfrac{1\times 3\times 5\times \ldots \times (2l+1)}{2^l l!(2l+1)^3} \left(\dfrac{R_{\rm M}}{r}\right)^{2l+1} & \text{for } r \geq R_{\rm M}, \end{cases} \tag{A1}$$

$$V_0^2 = \frac{\pi}{2} G(1+f) \frac{M_{\rm disk}}{R_{\rm M}}, \tag{A2}$$

where f is as defined earlier, and $M_{\rm disk}$ is the disk mass. The disk surface density is given by

$$\mu_{d,0} = \frac{V_0^2 \cos^{-1}(r_0/R_{\rm M})}{\pi^2 G r_0 (1+f)}. \tag{A3}$$

The code uses a finite polar grid. For $R_{\rm M}$ several times r_0, $\mu_{d,0}$ and $\Phi(r)$ are both close to those of the infinite Mestel disk. The $R_{\rm M}$ that we use is always taken to be several times larger than the inner ring, r_0. Our simulations cannot include an infinite disk without unrealistically assuming an inert disk beyond the grid radius. Our largest disk simulation fills $\sim$3/4 of the grid. Trials show that results are not sensitive to disk radius. The number distribution in the polar bins determines the potential. At each time step a discrete Fourier transform scheme computes the potential at each grid point; then the code performs a nine grid-point interpolation around each particle to determine the force on the particle. Finally, a time-centered semi-implicit leapfrog scheme determines the future position and velocity for each particle from its current position and velocity.

The grid uses 24 radial grid points according to the $r = Le^{\alpha u}$, where $\alpha = 2\pi/36$ and $u = 0$–24. There are 36 equal azimuthal grid points at 10° intervals, resulting in approximately square bins. Near the center, where the surface density of particles is large, the bins are small. Near the grid edge, where the surface density of particles is small, the bins are large. This grid provides an optimal combination of the increasing spatial resolution from edge to center, with the corresponding reduction of small-number statistics (too few particles per bin near the edge). At the disk center, this polar grid matches the resolution of a 720×720 Cartesian grid without such a Cartesian grid's long CPU time and without the Cartesian grid's small-number statistics problems near the disk edge. Doubling this grid size gains us nothing in improved results and increases our computer usage to an unacceptable amount. The 36×24 grid is sufficient to follow any gross features. In a test against an independently written Cartesian code, it gives similar results for similarly perturbed disks, subject to the expected deficiencies—the Cartesian grid's poorer central resolution and statistical problems (Thomasson 1989).

The code uses soft gravity in its force law (Byrd et al. 1986a, 1986b). We choose a softening value of 0.63, which prevents any random variation of particle number from bin to bin from causing structure in the inner disk. Any lower value falls prey to statistical fluctuations, and too large a value for the softening slows the development of the inner structure during encounters with a companion. For example, a value of 1.6 for the softening tends to smooth the inner structure (within $\approx$5 units of center) without affecting the general evolution of the shape. Clustering of outer material is more pronounced with larger values of the softening. For this study, we confine the primary galaxy to a plane, as discussed earlier. The time per simulation time step is

$$\Delta T \approx \frac{2\pi R_{\rm M}({\rm kpc})}{314 V_0({\rm km\ s^{-1}})} 10^9 \text{ yr}. \tag{A4}$$

Sundelius et al. (1987) introduced two disk components. One begins "cold," with a small velocity dispersion to represent disk gas clouds. The other begins "warm," with a velocity dispersion just equal to the critical value for stability against axisymmetric disturbances. This will represent old disk stars. Gas cloud particles in the same bin are presumed to exert damping forces on one another during each time step, i.e., all gas cloud particles receive their bin average vector velocity at the end of the time step. These are not true inelastic collisions with a particle at the grid center, in that the particles do not fuse together to make a single larger particle at the grid center. Under shearing and perturbation, the particles may separate from their bin neighbors in the future, but while they travel together they form a temporary, coherent cloud complex. If the density is large enough, gravitation will cause them to aggregate. The grid for collisions is the same grid used in the program, except that the subdivision into bins is finer, azimuthally every 5° rather than every 10°. To avoid small-number statistical effects, we require a critical number in a bin before collisions occur. We found that 10 particles in a bin was a good choice; lower values permit the enhancement of random fluctuations. This algorithm is simple, but it suits our purposes for studying the effects of gas cloud collisions.

In the present paper, we introduce a turning bar disk perturbation potential, as described earlier. We ran simulations of the time evolution of isolated disks for times equal to those of the perturbed bar simulations. The n bodies begin in equilibrium. A disk with no disturbance should develop little structure. As we hoped, there is very little development of rings or patterns when our n-body disk evolves in isolation. These tests had $f = 1.5$, with much more self-gravity and gravitational instability than in our NGC 3081 simulation.

REFERENCES

Arfken, G. 1985, Mathematical Methods for Physicists (3rd Ed.; New York: Academic Press), 711
Athanassoula, E. 1984, Phys. Rep., 114, 319
Binney, J., & Tremaine, S. 1987, Galactic Dynamics (Princton: Princeton Univ. Press)
Block, D. L., Buta, R., Knapen, J. H., Elmegreen, D. M., Elmegreen, B. G., & Puerari, I. 2004, AJ, 128, 183
Bruzual, G., & Charlot, S. 1996, AAS CD-ROM, Vol. 7 (Chicago: Univ. Chicago Press), http://www.journals.uchicago.edu/AAS/cdrom/volume7/
Buta, R. 1995, ApJS, 96, 39 (CSRG)
———. 1999, Ap&SS, 269, 79
———. 2002, in ASP Conf. Ser. 275, Disks of Galaxies: Dynamics and Perturbations, ed. E. Athanassoula, A. Bosma, & R. Mujica (San Francisco: ASP), 185

Buta, R., & Block, D. L. 2001, ApJ, 550, 243
Buta, R., Block, D. L., & Knapen, J. H. 2003, AJ, 126, 1148
Buta, R., Byrd, G., & Freeman, T. 2004a, AJ, 127, 1982 (Paper I)
Buta, R., & Combes, F. 1996, Fundam. Cosm. Phys., 17, 95
———. 2000, in ASP Conf. Ser. 197, Dynamics of Galaxies from the Early Universe to the Present, ed. F. Combes, G. A. Mamon, & V. Charmandaris (San Francisco: ASP), 15
Buta, R., & Crocker, D. A. 1991, AJ, 102, 1715
———. 1993, AJ, 105, 1344
Buta, R., Laurikainen, E., & Salo, H. 2004b, AJ, 127, 279
Buta, R., & Purcell, G. 1998, AJ, 115, 484
Byrd, G. G. 1995, Ann. NY Acad. Sci., 773, 302
Byrd, G. G., Rautiainen, P., Salo, H., Buta, R., & Crocker, A. 1994, AJ, 108, 476
Byrd, G. G., Saarinen, S., &Valtonen, M. 1986a, MNRAS, 220, 619
Byrd, G. G., Smith, B. F., & Miller, R. H. 1984, ApJ, 186, 62
Byrd, G. G., & Sundelius, B. 1986b, A&A, 166, 75
Combes, F., & Sanders, R. H. 1981, A&A, 96, 164
Contopoulos, G. 1979, in Photometry, Kinnematics and Dynamics of Galaxies, ed. D. D. Evans (Austin: Dept. of Astronomy, Univ. of Texas), 425
———. 1996, in IAU Colloq. 157, Barred Galaxies, ed. R. Buta, D. A. Crocker, & B. G. Elmegreen (ASP Conf. Ser. 91; San Francisco: ASP), 454
de Grijs, R. 1998, MNRAS, 299, 595
Freeman, T., & Byrd, G. 2000, in ASP Conf. Ser. 209, Small Galaxy Groups, ed. M. Valtonen & C. Flynn (San Francisco: ASP), 325
Gilmore, G., King, I., & van der Kruit, P. 1990, The Milky Way as a Galaxy (Mill Valley: University Science Books)
Goldreich, P., & Tremaine, S. 1981, ApJ, 243, 1062
Holmberg, J., & Flynn, C. 2004, MNRAS, 352, 440
Howard, S., Keel, W. C., Byrd, G., & Burkey, J. 1993, ApJ, 417, 502
Kalnajs, A. 1965, Ph.D. thesis, Harvard Univ.
———. 1991, in Dynamics of Disk Galaxies, ed. B. Sundelius (Göteborg: Göteborg Univ.), 323
Kormendy, J., & Kennicutt, R. C., Jr. 2004, ARA&A, 42, 603
Laurikainen, E., & Salo, H. 2002, MNRAS, 337, 1118
Lin, C. C., & Shu, F. H. 1966, Proc. Nat. Acad. Sci. US, 55, 229
Lynden-Bell, D., & Pineault, S. 1978, MNRAS, 185, 679
Mestel, L. 1963, MNRAS, 126, 553
Mihalis, D., & Routly, M. 1968, Galactic Astronomy (San Francisco: W. H. Freeman)
Miller, R. H. 1968, ApJ, 151, 699
———. 1970, ApJ, 161, 903
———. 1971, Ap&SS, 14, 73
———. 1974, ApJ, 190, 539
Patsis, P. A., Skokos, C., & Athanassoula, E. 2003, MNRAS, 346, 1031
Persic, M., Salucci, P., & Stel, F. 1996, MNRAS, 281, 27
Purcell, G., & Buta, R. 1996, in ASP Conf. Ser. 91, Barred Galaxies, ed. R. Buta, D. A. Crocker, & B. G. Elmegreen (San Francisco: ASP), 244
Quillen, A. C., & Frogel, J. A. 1997, ApJ, 487, 603
Quillen, A. C., Frogel, J. A., & González, R. A. 1994, ApJ, 437, 162
Rautiainen, P., & Salo, H. 2000, A&A, 362, 465
Regan, M., & Teuben, P. 2004, ApJ, 600, 595
Salo, H., Rautiainen, P., Buta, R., Purcell, G. B., Cobb, M. L., Crocker, D. A., & Laurikainen, E. 1999, AJ, 117, 792
Schwarz, M. P. 1981, ApJ, 247, 77
———. 1984, MNRAS, 209, 93
Sundelius, B., Thomasson, M., Valtonen, M., & Byrd, G. G. 1987, A&A, 174, 67
Thomasson, M. 1989, Research Report No. 162, Department of Radio and Space Science (Gothenburg: Onsala Space Obs./Chalmers Univ. Technology), 30
Toomre, A. 1981, in Structure and Evolution of Normal Galaxies, ed. S. M. Fall & D. Lynden-Bell (Cambridge: Cambridge Univ. Press), 67
van der Kruit, P. C. 1988, A&A, 192, 117
Worthey, G. 1994, ApJS, 95, 107